



# Statistical Properties of the Nebular Spectra of 103 Stripped-envelope Core-collapse Supernovae\*

Qiliang Fang (方其亮)<sup>1</sup>, Keiichi Maeda<sup>1</sup>, Hanindy Kuncarayakti<sup>2,3</sup>, Masaomi Tanaka<sup>4</sup>, Koji S. Kawabata<sup>5</sup>, Takashi Hattori<sup>6</sup>, Kentaro Aoki<sup>6</sup>, Takashi J. Moriya<sup>7,8</sup>, and Masayuki Yamanaka<sup>9</sup>

<sup>1</sup> Department of Astronomy, Kyoto University, Kitashirakawa-Oiwake-cho, Sakyo-ku, Kyoto 606-8502, Japan; [fangql@kustro.kyoto-u.ac.jp](mailto:fangql@kustro.kyoto-u.ac.jp)

<sup>2</sup> Tuorla Observatory, Department of Physics and Astronomy, FI-20014 University of Turku, Finland

<sup>3</sup> Finnish Centre for Astronomy with ESO (FINCA), FI-20014 University of Turku, Finland

<sup>4</sup> Astronomical Institute, Tohoku University, Sendai 980-8578, Japan

<sup>5</sup> Hiroshima Astrophysical Science Center, Hiroshima University, Kagamiyama, Higashi-Hiroshima, Hiroshima 739-8526, Japan

<sup>6</sup> Subaru Telescope, National Astronomical Observatory of Japan, 650 North A'ohoku Place, Hilo, HI 96720, USA

<sup>7</sup> National Astronomical Observatory of Japan, National Institutes of Natural Sciences, 2-21-1 Osawa, Mitaka, Tokyo 181-8588, Japan

<sup>8</sup> School of Physics and Astronomy, Faculty of Science, Monash University, Clayton, Victoria 3800, Australia

<sup>9</sup> Okayama Observatory, Kyoto University, 3037-5 Honjo, Kamogata-cho, Asakuchi, Okayama 719-0232, Japan

Received 2021 July 21; revised 2022 January 25; accepted 2022 January 25; published 2022 April 4

## Abstract

We present an analysis of the nebular spectra of 103 stripped-envelope (SE) supernovae (SNe) collected from the literature and observed with the Subaru Telescope from 2002 to 2012, focusing on [O I]  $\lambda\lambda$ 6300, 6363. The line profile and width of [O I] are employed to infer the ejecta geometry and the expansion velocity of the inner core; these two measurements are then compared with the SN subtypes, and further with the [O I]/[Ca II] ratio, which is used as an indicator of the progenitor CO core mass. Based on the best-fit results of the [O I] profile, the objects are classified into different morphological groups, and we conclude that the deviation from spherical symmetry is a common feature for all types of SESNe. There is a hint (at the  $\sim 1\sigma$  level) that the distributions of the line profile fractions are different between canonical SESNe and broad-line SNe Ic. A correlation between [O I] width and [O I]/[Ca II] is discerned, indicating that the oxygen-rich material tends to expand faster for objects with a more massive CO core. Such a correlation can be utilized to constrain the relation between the progenitor mass and the kinetic energy of the explosion. Further, when [O I]/[Ca II] increases, the fraction of objects with Gaussian [O I] profile increases, while those with double-peaked profile decreases. This phenomenon connects ejecta geometry and the progenitor CO core mass.

*Unified Astronomy Thesaurus concepts:* Core-collapse supernovae (304); Transient sources (1851)

## 1. Introduction

When the central nuclear fuel is exhausted, a massive star ( $\gtrsim 8 M_{\odot}$ ) will suffer from core collapse, resulting in a core-collapse supernova (CCSN), expelling the material above the core. The explosion energy and the geometry of the ejecta of this catastrophic event, together with their relations with the properties of the progenitor, are important factors for understanding the final evolution of massive stars.

Before an SN explodes, the massive star progenitor may suffer from a certain degree of envelope stripping either by binary evolution or stellar wind, or the combination of both (Heger et al. 2003; Groh et al. 2013; Smith 2014; Yoon 2015; Fang et al. 2019). If the hydrogen envelope is mostly retained before the explosion, the star will explode as a type II supernova (SN II), with strong hydrogen features in its spectra. Otherwise it will explode as a stripped-envelope supernova (SESN). SESNe can be further classified into type IIB SNe (SNe IIB; with strong hydrogen lines in early-phase spectra, which are later replaced by helium lines), type Ib SNe (SNe Ib; with spectra dominated by helium lines, showing no or weak hydrogen signatures), and type Ic SNe

(SNe Ic; with spectra lacking both hydrogen and helium lines). Type Ic SNe can be further divided into normal SNe Ic and broad-line type Ic (SNe Ic-BL). The early-phase spectra of the latter type show broad absorption features, indicating fast-expanding ejecta (by a factor of  $\sim 2$  faster than normal SNe Ic at maximum brightness) and large kinetic energy ( $\gtrsim 10^{52}$  erg, compared with  $\sim 10^{51}$  erg for typical SNe). SNe Ic-BL are sometimes associated with gamma-ray bursts (GRBs; see Galama et al. 1998; Hjorth et al. 2003; Woosley & Bloom 2006 for a review).

The explosion mechanism of CCSNe is an important open problem in modern astronomy. It is not yet clear how the gravitational energy is transformed to the kinetic energy of the outward-moving material. Placing observational constraints on the explosion geometry is one of the keys to answering this problem. The explosion energy may also depend on the progenitor masses (Ugliano et al. 2012; Müller et al. 2016; Sukhbold et al. 2016). Therefore, it is important to explore possible relations between these quantities from observational data; we thus need to have indicators of the kinetic energy, the ejecta geometry, and the progenitor mass independently from observables. For the mass of the progenitor star, the most robust method is to use a high-resolution image of the progenitor, although it still depends on the theoretical calculation of stellar evolution and therefore introduces some uncertainties (Smartt 2009 and Smartt 2015). The direct detection of the progenitors is only feasible in a relatively small volume, where CCSNe are rare events. The direct images of CCSNe are only available for a few number of cases, especially those lacking hydrogen-poor SNe (Maund et al. 2004, 2011;

\* This research is based (in part) on data collected at Subaru Telescope, which is operated by the National Astronomical Observatory of Japan.

Van Dyk et al. 2014; Folatelli et al. 2015; Kilpatrick et al. 2017; Tartaglia et al. 2017). For reviews, see Smartt (2009, 2015). So far only two SNe Ib, iPTF 13bvn and SN 2019yvr, have been identified (Cao et al. 2013; Kilpatrick et al. 2021).

SNe in their early phases are luminous enough so that they can be observed in distant galaxies. The luminosity scale and the shape of the light curve are dependent on the amount of radioactive elements, and the mass and the kinetic energy of the ejecta. The light-curve shape is also affected by how the radioactive power source is mixed in the envelope. Many works have been conducted that allow investigation of a possible relation between the ejecta mass and the explosion energy based on large samples (Drout et al. 2011; Dessart et al. 2016; Lyman et al. 2016; Prentice et al. 2016; Taddia et al. 2018). However, the early-phase emission mainly originates from the outermost region of the optical thick ejecta, and is not directly related to the inner core; thus, converting the ejecta mass estimated in this way to the progenitor mass may involve a large uncertainty. Further, the early-phase observables are generally not sensitive to the ejecta geometry except for the polarization signal (Wang et al. 2001; Wang & Wheeler 2008; Nagao et al. 2021). Indeed, most of the codes employed to model the early-phase SN light curve assume that the ejecta are spherically symmetric, which is not necessary valid (Maeda et al. 2008; Taubenberger et al. 2009).

Observation during the nebular phase naturally meets all of the requirements. After the massive star explodes, the density of the ejecta decreases with time following the expansion. At the same time, recombination also reduces the electron density. These effects together reduce the optical depth of the ejecta. When the ejecta becomes transparent to expose the inner region, the SN enters its nebular phase, and the spectrum is dominated by emission lines, most of which are forbidden lines. An SN usually enters its nebular phase several months to about one year after the explosion, depending on the physical conditions of the ejecta. For SNe II that retain most of their hydrogen envelope before the explosion, the nebular phase usually starts later than their envelope-stripped counterparts (SN I Ib/Ic).

The optically thin nature of the late-time ejecta allows for a nonbiased view on the entire ejecta, especially sensitive to the innermost region. One can therefore obtain indications of the geometry, the mass, and the expansion velocity of the innermost core, using the same late-phase data. The width of an emission line, together with its profile, allows one to explore the velocity scale and the geometry of the emitting region. The absolute or relative strength of emission lines is also related to the mass, volume, and physical conditions of the emitting regions (Fransson & Chevalier 1989; Jerkstrand et al. 2015; Jerkstrand 2017; Dessart et al. 2021). The information thus obtained can be utilized to infer the properties of the progenitor and constrain the explosion mechanism.

In this work, we conduct a study on the properties of the emission lines, including the width, profile, and strength based on the so-far largest sample of SESN nebular spectra. In the sample, 88 spectra are collected from the literature, and 15 spectra are newly presented from the observations carried out with the Subaru Telescope from 2002 to 2012. In the present work, we focus on the forbidden line [O I]  $\lambda\lambda 6300,6364$ , as it is one of the most luminous emission lines in the optical window of SESN nebular spectra. Further, oxygen is one of the most abundant elements in the ejecta of SESNe, and the [O I] dominates the emission from the CO core; the [O I]  $\lambda\lambda 6300,6364$  doublet is thus an ideal tool

to trace the geometry of the ejecta and the properties of the progenitor.

The paper is organized as follows. In Section 2, the full sample, the data reduction methods, and the measurement of the observables are introduced. The latter includes the width and line profile of the [O I]  $\lambda\lambda 6300,6364$ , and the line ratio [O I]  $\lambda\lambda 6300,6364$ /[Ca II]  $\lambda\lambda 7291,7323$ . In Section 3, we perform statistical analysis on the line profile. The statistics of the [O I]/[Ca II] ratio as well as its correlations with other observables, including the [O I] width and the line profile, are presented in Section 4. Section 5 is devoted to the physical implications of the statistical results of Sections 3 and 4. The validity and the possible affecting factors of the measurements are discussed in Section 6. Finally, the conclusions are given in Section 7.

## 2. Data Set

### 2.1. Sample Description

The sample in this work includes the late-time spectra of 103 SESNe (26 SNe I Ib, 31 SNe Ib, 32 SNe Ic, 9 SNe Ic-BL, and 5 SNe Ib/c), among which 15 objects are not published in the previous literature. The spectra are selected if the signal-to-noise level is acceptable, and the wavelength covers 6000–8000 Å so that the measurements in this work ([O I] and [Ca II]) are possible. The phases of the spectra are restricted to later than 100 days after the explosion or the peak luminosity (if the light curve is available). The objects that are decidedly nebular are also included, even if early-phase observations do not exist and the exact phase is unknown. If multiple nebular spectra are available for a specific object, we pick the one closest to 200 days. However, the quantities of interest in this work ([O I]/[Ca II] and the [O I] width) are not sensitive to the spectral phase within the range used here, so the effect of temporal evolution is generally negligible (see Maurer et al. 2010 and Fang et al. 2019 for the time evolutions of [O I] width and [O I]/[Ca II], respectively; see also the discussion in Section 6). The previously published spectra are collected from The Open Supernova Catalogue<sup>10</sup> (Guillochon et al. 2017) and WiseRep<sup>11</sup> (Yaron & Gal-Yam 2012). The full sample of this work is listed in Tables A1–A5 in Appendix A.

### 2.2. Data Reduction

For the new data set presented in this paper, the spectroscopic observations for the 15 SESNe were performed from MJD 52432 (2002 June 7) to MJD 56222 (2012 October 22) with the 8.2 m Subaru Telescope equipped with the Faint Object Camera and Spectrograph (FOCAS; Yoshida et al. 2000; Kashikawa et al. 2002). The typical instrumental setup is as follows: we used the 0''8 slit and the B300 (with no filter) and R300 (equipped with the O58 filter) grisms, or the 0''8 offset slit and the B300 grism equipped with the Y47 filter. The spectral resolution is  $\sim 500$ , or  $\sim 13$  Å at 6300 Å. The log of the observations is listed in Table 1.

The spectra are reduced following the standard procedures using IRAF<sup>12</sup> (Tody 1986, 1993), including bias subtraction, flat-fielding, sky subtraction, 1D spectral extraction,

<sup>10</sup> <https://sne.space/>

<sup>11</sup> <https://www.wiserep.org/>

<sup>12</sup> IRAF is distributed by the National Optical Astronomy Observatory, which is operated by the Association of Universities for Research in Astronomy, Inc., under cooperative agreement with the National Science Foundation. PyRAF is a product of the Space Telescope Science Institute, which is operated by AURA for NASA.

**Table 1**  
Log of Spectroscopic Observations with FOCAS

Object	Date YY/MM/DD	Instrumental Setup (grism/filter)	Exposure Time (s)
2005bj	05/08/25	B300off/Y47	3 × 1200
2005aj	05/10/26	B300off/Y47	2 × 1200
2006G	06/06/30	B300off/Y47	1 × 1200
2006ep	06/12/24	B300off/Y47	1 × 1200
2007D	07/09/18	B300off/Y47	2 × 1500
2007ay	07/11/05	B300off/Y47	1 × 1200
2008fo	09/04/05	B300cen, R300cen/O58	1 × 1200
2008fd	09/07/23	B300cen, R300cen/O58	1 × 1200
2008hh	09/08/18	B300cen, R300cen/O58	2 × 1000
2008im	09/08/18	B300cen, R300cen/O58	2 × 720
2009C	09/10/26	B300cen, R300cen/O58	2 × 900
2009K	09/10/26	B300cen, R300cen/O58	2 × 900
2008ie	09/10/27	B300cen, R300cen/O58	4 × 1200
2009jy	10/05/06	B300cen, R300cen/O58	2 × 1200
2009ka	10/05/06	B300cen, R300cen/O58	1 × 900

wavelength calibration using ThAr or HeNeAr lamps and skylines, and cosmic-ray rejection using LACosmic (van Dokkum 2001). Flux calibration is performed by using standard stars observed in the same night. The spectra are shown in Figure 1.

### 2.3. Measurement of Observables

The goal of this work is to investigate the physical properties of the ejecta and the progenitors, by using a large data set of nebular spectra of SESNe. In this work, we are not attempting to fit the nebular spectra with full spectral modeling; instead, several observables are employed as the indicators of the physical properties of the ejecta or the progenitor, including the line ratio of [O I]  $\lambda\lambda 6300, 6364$  to [Ca II]  $\lambda\lambda 7291, 7323$ , which is suggested to be related to the CO core mass, and thus the zero-age-main-sequence (ZAMS) mass of the progenitor (see later discussion). Following Taubenberger et al. (2009), the line profile and the width of [O I] are utilized to probe the geometry and velocity scale of the ejecta.

The nebular spectra of SESNe are dominated by [O I] and [Ca II] emissions. Before measuring the observables, a nebular spectrum is de-reddened and corrected for redshift at the first step. The color excess  $E(B - V)$  of the host galaxy and the Milky Way absorption are derived from previous literature (see the references in Tables A1–A5). For SNe without reported  $E(B - V)$ , the extinction is estimated from the equivalent width of Na ID absorption, using the relation derived from Turatto et al. (2003), if spectra around the light-curve peak are available. Otherwise  $E(B - V)$  is set to be 0.36 mag, which is the average value for SN Ib/c by Drout et al. (2011). The spectra are then corrected for extinction by applying the Cardelli law (Cardelli et al. 1989), assuming  $R_V = 3.1$ .

The redshifts for most objects are inferred from the central wavelength of the narrow emissions from their explosion sites ( $H\alpha$ , [N II], etc.). If such narrow lines are absent in the spectrum, the redshift of the host galaxy from HyperLeda<sup>13</sup> is adopted (Makarov et al. 2014).

The next step is to remove the underlying continuum emission. Following Fang et al. (2019), we first slightly smooth

the spectra and find the local minimum at both sides of the [O I]/ $H\alpha$ -like structure (also [Ca II]/[Fe II]) complex. A line connecting the two minima is defined to be the local continuum emission and is then subtracted. Indeed, the continuum of nebular-phase SNe is not real continuum emission, but made of thousands of weak overlapping lines (Li & McCray 1996; Dessart et al. 2021). Subtracting the straight line defined above may result in some residual, which therefore affects the measurement. However, as long as all objects are treated with the same method, the effect of the residual on statistics will be negligible. After these two steps, we can start to measure the line ratios and [O I] profiles.

1. [O I] and [Ca II]: The relative flux of [Ca II] is measured following the same procedure as in Fang et al. (2019). As for [O I], instead of fitting the [O I] with a double Gaussian function as illustrated in Fang et al. (2019), we assume the  $H\alpha$ -like structure located at the red side of [O I] is symmetric with respect to 6563 Å. Its profile is constructed by reflecting the red wing to the blue side with respect to 6363 Å, and the relative flux is then computed. The  $H\alpha$ -like structure is commonly seen in the nebular spectra of SNe IIB and some SNe Ib, and is identified as  $H\alpha$  or [N II] (Patat et al. 1995; Jerkstrand et al. 2015; Fang & Maeda 2018). As will be discussed in Section 6, the measured line width is not sensitive to the assumed symmetric center; therefore, the exact identification of this line is not important for the purpose of this work. Given that the symmetric center of the [N II] doublets is close to 6563 Å, to avoid further complication, we assume the excess emission is symmetric with respect to 6563 Å. After the  $H\alpha$ -like complex is subtracted, the profile and the relative flux of [O I] can be determined.
2. Line width of [O I]: The line width of [O I] is measured after the  $H\alpha$ -like structure is subtracted from the complex. We first define  $\lambda_c$ , such that the integrated fluxes at both sides are equal. We then find  $\lambda_{\text{blue}}$  and  $\lambda_{\text{red}}$ , where the integrated fluxes between  $\lambda_{\text{blue}} \dots \lambda_c$  and  $\lambda_c \dots \lambda_{\text{red}}$  take 34% of the total emission. The line width measured in this way defines  $1\sigma$  if the [O I] profile is Gaussian. A detailed example of line width measurement is presented in Figure 2. Throughout this work, the blue width  $\Delta\lambda_{\text{blue}}$  ( $\equiv \lambda_c - \lambda_{\text{blue}}$ ) is employed as the measurement of the line width, instead of using the half width  $\Delta\lambda_{\text{half}}$  ( $\equiv \frac{\lambda_{\text{red}} - \lambda_{\text{blue}}}{2}$ ) or the red width  $\Delta\lambda_{\text{red}}$  ( $\equiv \lambda_{\text{red}} - \lambda_c$ ). This is because  $\Delta\lambda_{\text{blue}}$  is less affected by the subtraction process or the profile of the  $H\alpha$ -like structure. A detailed discussion is left to Section 6.

The emission lines are broadened by the instrument. The measured line width can be corrected to account for the resolution of the instrument as

$$\Delta\lambda_{\text{intrinsic}} = \sqrt{\Delta\lambda_{\text{observed}}^2 - \Delta\lambda_{\text{narrow}}^2}, \quad (1)$$

where  $\Delta\lambda_{\text{intrinsic}}$ ,  $\Delta\lambda_{\text{observed}}$ , and  $\Delta\lambda_{\text{narrow}}$  are the intrinsic line width, observed line width, and the width of the narrow emission from the explosion site ( $H\alpha$ , [N II], etc.). Here, the width of the narrow emission reflects the instrumental broadening. According to the definition of  $\Delta\lambda_{\text{blue}}$ , the emission within this range takes 34% of the total flux, which is the same as  $1\sigma$  if the line is Gaussian. Therefore the narrow  $H\alpha$  is fitted

<sup>13</sup> <http://leda.univ-lyon1.fr/>

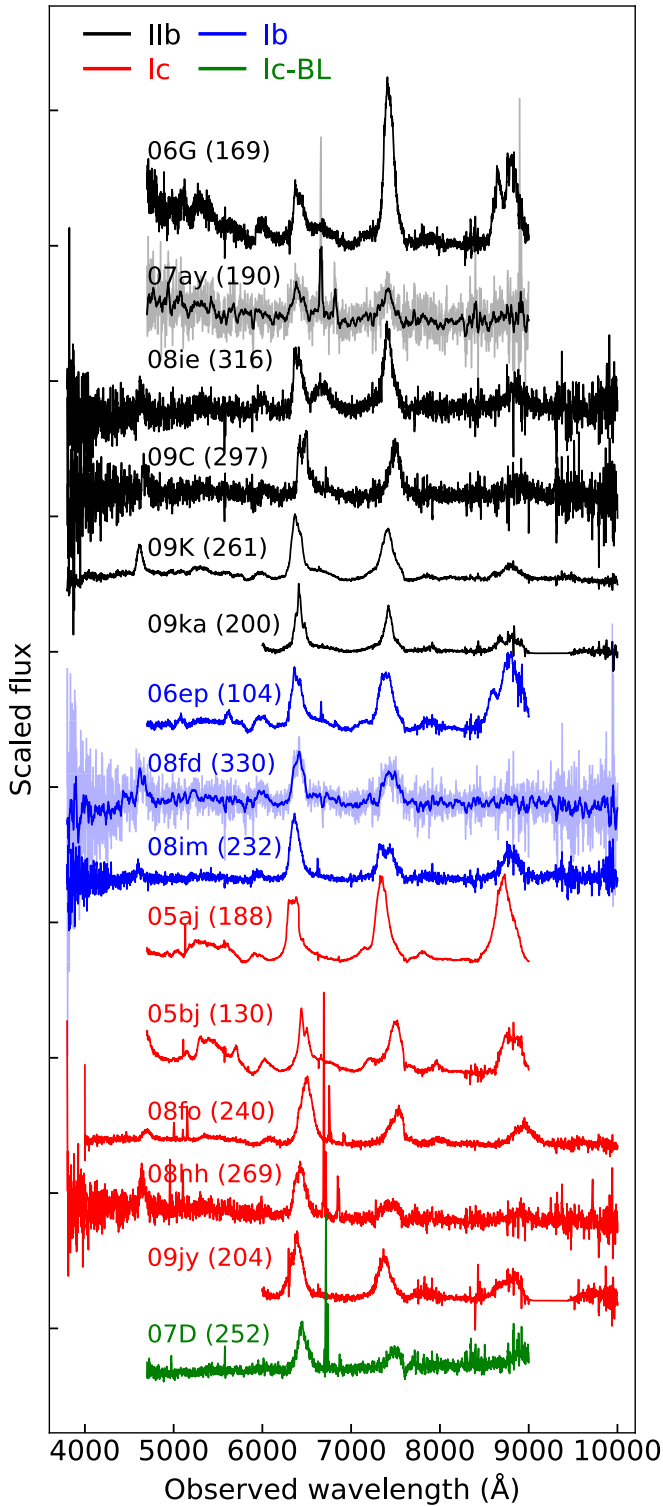


**Figure 1.** The nebular spectra of the Subaru/FOCAS objects. The fluxes of the spectra are first normalized, and then added by different constants for illustration. The objects are labeled by the last two digits of the discovery year and letter(s). The phase relative to the discovery date or light-curve maximum (if available) of each spectrum is listed in the parentheses (unit: days). SNe of different subtypes are plotted with different colors. SN2007ay and SN2008fd are smoothed for illustrative purposes.

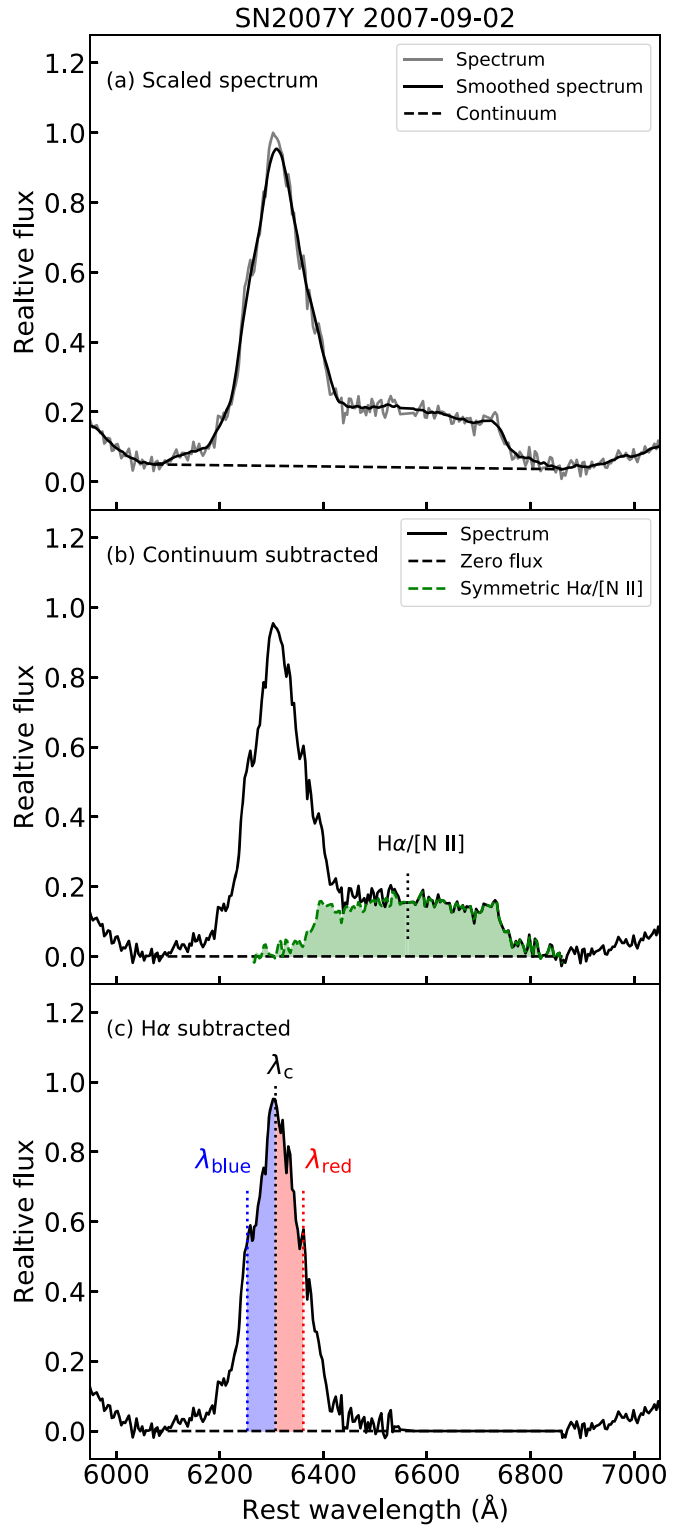


**Figure 2.** A detailed example of observable measurement in Section 2.3. The spectrum of SN2007Y is corrected for extinction and redshift, then multiplied by a constant for illustrative purposes. Upper panel: the spectrum is smoothed and the continuum level is determined as illustrated by the dashed line. Middle panel: the continuum is subtracted and the symmetric H $\alpha$ -like structure is constructed. Lower panel: the H $\alpha$ -like structure is subtracted. The line width is determined by  $\lambda_c - \lambda_{\text{blue}}$ .

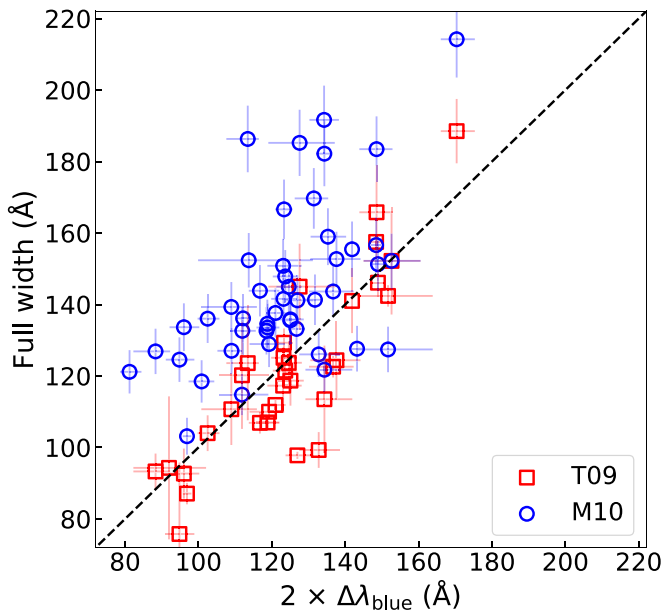


**Figure 3.** A comparison between the line width measure in this work and previous works. The red squares are for the FWHM from the one-component fit of Taubenberger et al. (2009, hereafter T09). The blue circles represent the line widths transformed from the  $v_{50}$  in Maurer et al. (2010, hereafter M10). The uncertainty is set to be 10%. The black dashed line is for one-to-one correspondence.

by a Gaussian function, and the derived variance  $\sigma$  is set to be  $\Delta\lambda_{\text{narrow}}$ . The narrow lines from the explosion site are absent for some objects in the sample. For these objects, the instrumental resolution is derived from the source paper, which is usually measured from the FWHM of the sky line, and transformed to the Gaussian  $\sigma$  as

$$\sigma = \frac{\text{FWHM}}{2\sqrt{2 \ln 2}}. \quad (2)$$

The average  $\Delta\lambda_{\text{narrow}}$  is  $4.02 \text{ \AA}$ , and the variation is  $1.87 \text{ \AA}$ .

The uncertainties of the measurements are estimated using a Monte Carlo method. A nebular spectrum is slightly smoothed at the first step by convolving with a boxcar filter. The smoothed version of the spectrum is then subtracted from the original one. The standard deviation at the range of  $6000\text{--}7800 \text{ \AA}$  of the residual flux is employed as the noise level of the spectrum. Ten-thousand simulated spectra are generated by adding noise on the smoothed spectrum. We further change the endpoints of the (continuum) background by the  $-25\text{--}25 \text{ \AA}$  range, which is assumed to be distributed uniformly with  $\Delta\lambda = 1 \text{ \AA}$  increments. The symmetry center of the  $\text{H}\alpha$ -like structure, initialized as  $6563 \text{ \AA}$ , is also allowed to be shifted by  $-45\text{--}45 \text{ \AA}$  following the uniform distribution. The above measurements of the observables are then performed on the simulated spectra. Finally the measured line width is corrected for the effect of instrumental broadening. The 84% and 16% of the results of the  $10^4$  measurements are taken as the upper and lower limits of the observables, respectively.

In Figure 3, the measured line widths are compared with those of the previous works with overlapping objects. For the comparison work, we take the result of the one-component fit of Taubenberger et al. (2009), and the FWHM from the full spectral modeling of Maurer et al. (2010). The measurement of the line width in this work agrees well with Taubenberger et al.

(2009), while it is systematically smaller than that in Maurer et al. (2010); however, a correlation can still be discerned, and the systematic offset may simply be due to different definitions of the line velocity/width. The line width measurement in this work does not assume the geometry or the detailed physical conditions of the [O I] emitting region, and thus allows for more general discussion on the velocity scale and structure of the ejecta than previous works.

#### 2.4. Fitting the [O I] $\lambda\lambda 6300, 6364$

After the background and the  $\text{H}\alpha$ -like structure are subtracted, the [O I] is fitted with multiple Gaussian profiles using the method described in Taubenberger et al. (2009). We define a single “doublet” component as two Gaussian functions with the same standard deviation, central wavelengths separated by  $3000 \text{ km s}^{-1}$ , and intensity ratio of 3:1, which is expected if the ejecta are optically thin. A single component has three parameters: the center wavelength  $\lambda_{\text{peak}}$ , the width  $\sigma$ , and the (scaled) intensity. The fitting procedure involves up to two components, and then we have five free parameters in total (note that one parameter is reduced since only the relative intensity matters).

The fitting starts from one component. If the residual exceeds the noise level, an additional component is introduced as follows. We first set four types of initial guesses: (1) two components red- and blueshifted by  $2000 \text{ km s}^{-1}$ , with  $\sigma = 1000 \text{ km s}^{-1}$  and the same intensity; (2) A broad component centered at  $v = 0 \text{ km s}^{-1}$  and  $\sigma = 2500 \text{ km s}^{-1}$ , with a narrow component ( $\sigma = 500 \text{ km s}^{-1}$ ) centered at  $v = 0 \text{ km s}^{-1}$ . The intensity of the narrow component is initialized to be 30% of the broad base; (3) Same as above, but with the narrow component centered at  $v = 2000 \text{ km s}^{-1}$ ; (4) Same as above, but with the narrow component centered at  $v = -2000 \text{ km s}^{-1}$ . We then start the fitting with these initials guesses. For case (1), the two components are forced to be blue- and redshifted by more than  $v = 1000 \text{ km s}^{-1}$  (resolution  $R \sim 300$ ), and the relative contribution of each component to the flux is forced to be  $\gtrsim 0.3$ ; otherwise, it is considered unacceptable. For cases (2), (3), and (4), the center of the broad base is allowed to vary within  $-1600\text{--}600 \text{ km s}^{-1}$ . Here the broad base is allowed to suffer from bulk blueshift up to  $1000 \text{ km s}^{-1}$  to account for the effect of residual opacity in the core of the ejecta (see Figure 3 of Taubenberger et al. 2009). The additional  $\pm 600 \text{ km s}^{-1}$  corresponds to a spectroscopic resolution of  $\sim 500$ . The result with the smallest residual is taken to be the final result.

According to the results, the line profiles are classified into four classes: Gaussian, narrow core, double-peaked, and asymmetric (hereafter GS, NC, DP, and AS, respectively). In the following, the definitions and the physical implications of the line profiles are briefly summarized. The readers may refer to Taubenberger et al. (2009) for more details. In Section 5.1, we will further discuss the expected profiles from a specific bipolar-type explosion, given as an example in the list below. Some examples of the line profiles are shown in Figure 4.

1. Gaussian (GS): The line can be well fitted by one component. The emitter is expected to originate from the Gaussian distribution in the radial direction of a spherically symmetric ejecta. While there is no need to introduce deviation from spherical symmetry to explain the GS profile, it does not reject a possible asphericity; for

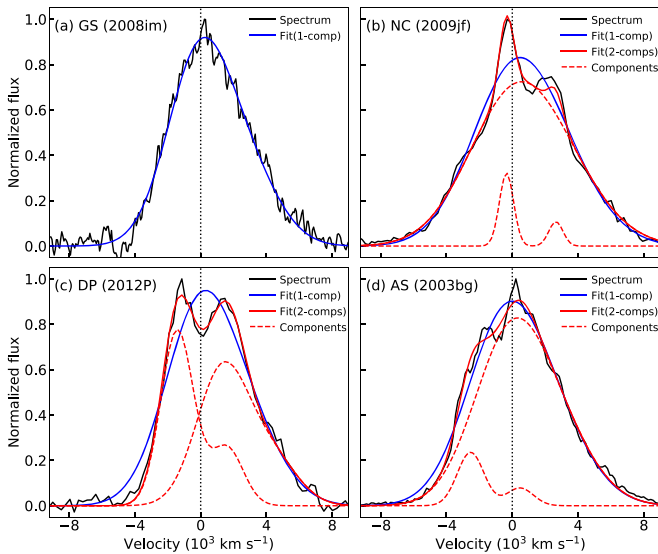


**Figure 4.** Examples of the four line profiles. Before the fitting procedure, the spectra are subtracted by the background and the symmetric  $H\alpha$ -like profile as described in the text. The red solid line is the result of the two components fit, and the red dashed lines are the corresponding components. The blue solid line represents the one component fit, and is also plotted in panels (b), (c), and (d) for comparison. In this work, we use the same classification scheme as Taubenberger et al. (2009).

example, a bipolar-type explosion (with the torus-like distribution of oxygen) viewed from the intermediate angle also results in a similar profile.

2. **Narrow core (NC):** The line can be fitted by two components: a broad base and a narrow additional one with very close center wavelengths (in this work, it is defined to be offset  $< 1000 \text{ km s}^{-1}$ ).<sup>14</sup> A straightforward interpretation is the emission from spherically symmetric ejecta with an enhanced core density. The axisymmetric configuration as described above but viewed from the polar direction (perpendicular to the O-rich torus) can also produce a similar profile. Indeed, the profile simply requires that there is a massive O-rich component with a negligible velocity along the line of sight, and thus even a single massive blob moving perpendicular to the line of sight is not rejected.
3. **Double-peaked (DP):** The line can be well fitted by two components with similar intensities, one blueshifted and the other redshifted by similar amounts (case (1) in the above text). If interpreted simply as a geometrical effect, this profile is not reproduced under the assumption of spherical symmetry, and requires two components having the symmetry in the line-of-sight velocity distribution. A simple configuration leading to this profile is the axisymmetric explosion mentioned above but viewed from the edge of the torus.
4. **Asymmetry (AS):** The line can be fitted by a broad component accompanied by an additional component with arbitrary width and shift of the center wavelength. This again requires a deviation from a pure spherically

<sup>14</sup> In Taubenberger et al. (2009), the narrow core is defined to have the narrow component with offset  $< 22 \text{ \AA}$  ( $\sim 1000 \text{ km s}^{-1}$ ) with respect to the *rest wavelength*. However, such offset can also be the result of residual opacity, which will affect both broad and narrow components, rather than pure geometrical effect. We therefore employ offset relative to the center of the *broad base* as the criterion for the narrow core.

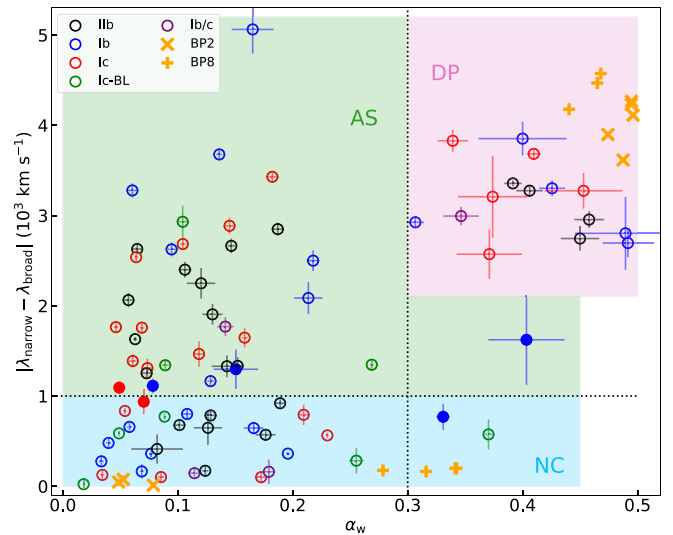


**Figure 5.** The fractional flux of the secondary component is plotted against the central wavelength's separation. Different [O I] profile classes are well separated by  $\alpha_w = 0.3$  and  $|\lambda_1 - \lambda_2| = 1000 \text{ km s}^{-1}$  (the dotted lines). Objects of different profile classes are labeled by different colors and markers. BP2 and BP8 are the bipolar explosion models in Maeda et al. (2008) with different degrees of axisymmetry. We apply the same fitting procedure as described in Section 2.4 to the theoretical spectra. See Section 5.1 for detailed descriptions on the BP models.

symmetric ejecta, pointing to the existence of a single dominating blob corresponding to the narrow component, in addition to the bulk distribution representing the broad component. It should be noted that the only difference between NC and AS is the relative shift of the narrow component. Whether NC/AS are distinct populations is not clear. See the statistic results in Sections 3.1 and 6.3.

Most of the objects in the sample can be well fitted by the method applied in this work (see Figures B1–B4 in Appendix B), although some objects, e.g., SN 2006ld and SN 2008aq, possibly require more complicated ejecta geometry.

### 3. Statistics of the [O I] Profile

The profile of the emission line is a useful tracer of the geometry of the ejecta (e.g., Taubenberger et al. 2009). Although it is not possible to recover the full 3D distribution of the emitter, the measurement in this work can still provide some information on any possible deviation from spherical symmetry. The classifications of [O I] line profiles are listed in Tables A1–A5.

#### 3.1. Quantitative Classification

To quantify the difference between the classifications, for objects fitted by two components ( $N = 82$ ), in Figure 5, the fractional flux of the secondary component  $\alpha_w$ , which is defined to be the component with the smaller flux, is plotted against the absolute central wavelength offset between the two components. Similarly to Figure 6 of Taubenberger et al. (2009), objects of different line profile classes, by definition, occupy different regions in the plot and are well separated. NC objects are characterized by a narrow strip located in the lower-left region ( $\alpha_w \lesssim 0.4$ ,  $|\lambda_1 - \lambda_2| < 1000 \text{ km s}^{-1}$ ). The DP and AS objects have wider central wavelength separation, and are

**Table 2**  
Statistics of the [O I] Profile

Types	Full	I Ib <i>N</i> (fraction)	Ib	Ic	Ib/c	Ic-BL
GS	21(0.20)	3(0.12)	7(0.23)	9(0.28)	1(0.20)	1(0.11)
NC	30(0.29)	7(0.27)	9(0.29)	7(0.22)	2(0.40)	5(0.56)
DP	16(0.16)	4(0.15)	5(0.16)	5(0.16)	1(0.20)	0(-)
AS	36(0.35)	12(0.46)	10(0.32)	11(0.34)	1(0.20)	3(0.33)

separated at  $\alpha_w \sim 0.3$ . It should be emphasized that the boundary between NC and AS is changeable. In this work, we choose the same criterion as Taubenberger et al. (2009), i.e., offset = 1000 km s<sup>-1</sup> ( $\sim 22 \text{ \AA}$ ). Moreover, the uncertainty of the fitting allows some objects, especially those near the boundary, to be reclassified to the other category. Objects with nonnegligible probability ( $>0.05$ ) of shifting to the other category are labeled by filled markers in Figure 5.

According to the classification of Taubenberger et al. (2009), objects with narrow component shifts smaller (or larger) than 1000 km s<sup>-1</sup> are classified as NC (or AS). However, as shown in Figure 5, the narrow component shift has a continuous distribution, and it is questionable whether NC and AS are two distinct populations. A more detailed discussion on the classification of NC/AS is left to Section 6.3.

### 3.2. Statistical Evaluation

The fractions of the line profiles are shown in Table 2. In the sample of this work, the fractions of GS, NC, DP, and AS objects are: 0.20 ( $N = 21$ ), 0.29 ( $N = 30$ ), 0.16 ( $N = 16$ ), and 0.35 ( $N = 36$ ), respectively. The large fraction of AS/DP objects suggests that the deviation from spherical symmetry is common for the ejecta of SESNe. These two categories require the deviation from spherical symmetry, and thus place a lower limit of  $\sim 50\%$  on SESNe having nonspherical ejecta (note that the other two categories, GS/NC, can be explained by, but do not require, spherically symmetric ejecta; Section 2.4). This finding is consistent with previous studies (Maeda et al. 2008; Modjaz et al. 2008; Taubenberger et al. 2009; Milisavljevic et al. 2010). The line profile fractions are generally in good agreement with the results of Taubenberger et al. (2009). Given that the fractions show no significant variation after the sample is enlarged by a factor of 2.5 (39 objects in Taubenberger et al. 2009 and 103 objects in this work), we conclude that the distribution of [O I] profiles, which is directly linked to the ejecta geometry, is already statistically well determined, and can be a potential constraint on the explosion mechanism.

The distributions of the line profiles of different SN subtypes, along with the full sample for comparison, are shown in Figure 6. In general, the line profile distributions of the canonical SESNe (I Ib/Ib/Ic) are quite similar to each other. The uncertainties of the fractions of different line profiles in different SN subtypes are estimated by a bootstrap-based Monte Carlo method. We run  $10^4$  simulations. In each trial, the SNe sample is resampled with replacement. For NC and AS objects, the probability of reclassification into the other category is also included (see Section 3.1). The fractions of different line profiles of the new sample and the different SN subtypes are then calculated. The 16% and 84% levels of the  $10^4$  trials are employed as the lower and upper limits of the line profile fractions, respectively.

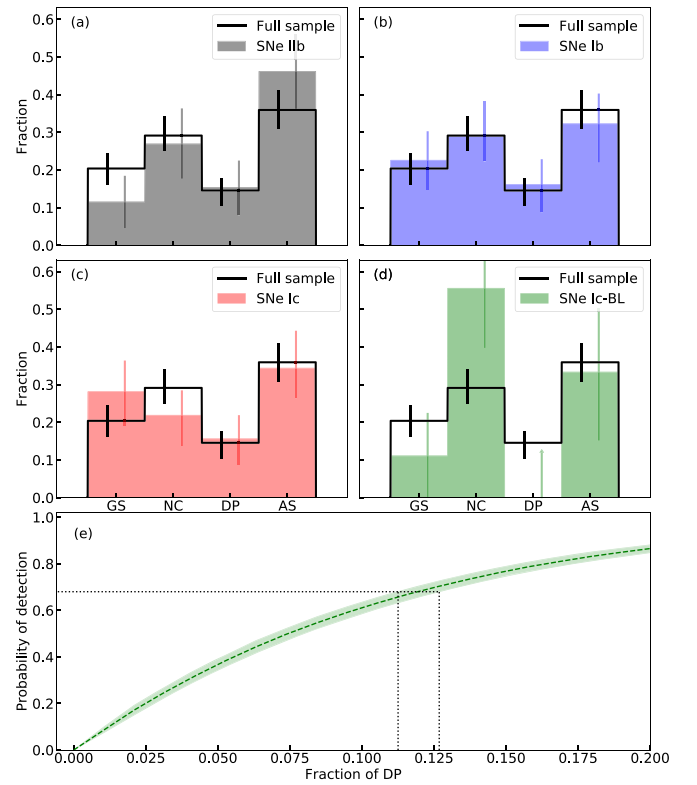


**Figure 6.** (a)–(d) The distributions of the [O I] profile of different SN subtypes, which are shown in different colors and panels. The histogram plotted by the black solid line is the distribution of the full sample. The error bars are estimated by the bootstrap Monte Carlo method described in the main text. The  $1\sigma$  upper limit of the DP fraction of SNe Ic-BL is marked by the arrow in panel (d). In panel (e), the probability for DP detection as a function of intrinsic DP fraction for SNe Ic-BL is shown. The shaded region represents the 95% CI. The vertical dotted lines mark the range of  $f_{DP}$  such that the probability of detection is equal to 0.68.

Taubenberger et al. (2009) suggested the objects with an extended envelope tend to be more aspherical, as the SNe Ib in their sample mainly belong to the AS category. The results in this work do not support their finding. Although the fraction of AS objects in the SNe Ib sample is slightly larger than the average, we find no significant difference in the line profile distributions among SNe Ib/Ib/Ic. The similarity likely indicates a limited effect of the presence of the helium layer or the residual hydrogen envelope on the ejecta geometry. For each subtype, at least 50% (and likely more) of the objects can not be interpreted by the spherical symmetric ejecta, and such deviation is commonly seen for all types of canonical SESNe.

Some differences of SNe Ic-BL when compared with the average behavior can be discerned: (1) large fraction of NC objects, and (2) lack of DP objects. However, in this work, the number of SNe Ic-BL is small ( $N = 9$ ). The lack of DP objects can be the result of small-sample statistics. We therefore need to estimate the upper limit of the intrinsic DP fraction above which the nondetection is statistically significant. For this purpose, we run  $10^4$  simulations. In each trial, the GS, NC, and AS fractions ( $f_{GS}$ ,  $f_{NC}$ , and  $f_{AS}$ ) are randomly drawn from the full sample with the bootstrap-based Monte Carlo method introduced above. The intrinsic DP fraction  $f_{DP}$  is varied from 0 to 0.2, with the ratio of  $f_{GS}$ ,  $f_{NC}$ , and  $f_{AS}$  kept fixed. For the fixed  $f_{DP}$ ,  $10^3$  samples (size  $N = 9$ ) are generated according to the current line profile distribution. The rate of the samples with DP detected is then calculated. The relation between the DP

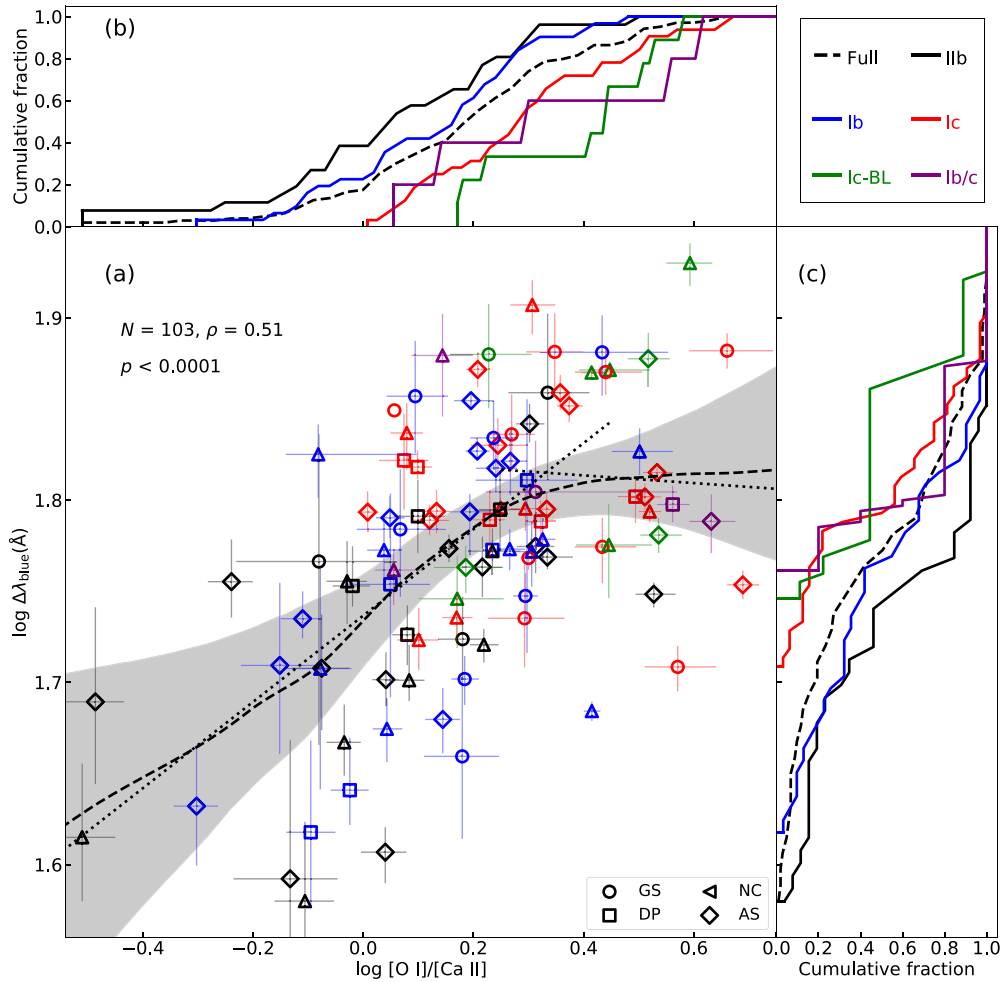


**Figure 7.** (a) The relation between the  $[\text{O I}]/[\text{Ca II}]$  ratio and the  $[\text{O I}]$  width  $\Delta\lambda_{\text{blue}}$ . SESNe of different SN subtypes and line profile classes are labeled by different colors and markers. The black dashed line is the result of the local nonparametric regression for the full sample, and the shaded region represents the 95% CI. The black dotted lines are the results of the linear regression performed for the objects with  $\log [\text{O I}]/[\text{Ca II}] < 0.4$  and  $\log [\text{O I}]/[\text{Ca II}] > 0.4$ , respectively. (b) Cumulative fraction of the  $[\text{O I}]/[\text{Ca II}]$  ratio. (c) Cumulative fraction of the  $[\text{O I}]$  width  $\Delta\lambda_{\text{blue}}$ .

fraction and the detection probability are shown by the green dashed line in Figure 6(e). The shaded region is the 95% confidence interval (CI) of the  $10^4$  simulations. When  $f_{\text{DP}} = 0$ , no DP object can be detected in all trials by definition. As  $f_{\text{DP}}$  increases, the probability of detection increases as expected. The upper limit of  $f_{\text{DP}}$  is defined to be the value such that detection probability  $p_{\text{detect}} = 0.68$  (or nondetection probability = 0.32). This  $1\sigma$  upper limit ranges from 0.112 to 0.126 (mean value = 0.119), as indicated by the vertical dotted lines in Figure 6(e). The conservative value 0.126 is employed as the upper limit of the DP fraction of SNe Ic-BL, which is still smaller than the DP fraction (0.155) of the full sample, but slightly larger than its lower limit (0.120). Therefore, there is an indication, at a confidence level of about  $1\sigma$ , that the lack of double-peaked SNe Ic-BL is an intrinsic feature rather than statistical effect.

A hint that the distribution of the line profiles of SNe Ic-BL is different from those of the canonical SESNe can thus be discerned, which suggests a difference in ejecta geometry. From early-phase observation, SNe Ic-BL are already found to be distinct from other SESNe with their extreme nature. The finding in this work further extends such distinction in the nebular phase.

The full sample is large enough for statistical evaluation. However, the size of each SNe subtype is still limited, especially lacking SNe Ic-BL. Inferences made based on the fractions of small samples are uncertain (Park et al. 2006). To reliably investigate the dependence of the line profiles on SNe subtypes, an even larger sample is required.

#### 4. $[\text{O I}]/[\text{Ca II}]$ and $[\text{O I}]$ Width

The individual measurements of the  $[\text{O I}]/[\text{Ca II}]$  ratio and the  $[\text{O I}]$  width  $\Delta\lambda_{\text{blue}}$  for each object in the sample is plotted in Figure 7(a). The cumulative distributions of these two quantities are plotted in panels (b) and (c), respectively, where the objects of different SN subtypes are labeled by different colors, and the cumulative fraction of the full sample is labeled by the black dashed line. Objects of different line profile classes (i.e., GS, NC, DP, and AS; see the previous section for details) are discernible by different markers.

##### 4.1. Statistical Evaluation

Similarly to the result in Fang et al. (2019), for  $[\text{O I}]/[\text{Ca II}]$ , an increasing sequence is discerned: SNe I Ib/Ib  $\rightarrow$  SNe Ic  $\rightarrow$  SNe Ic-BL. Although compared with the results in Fang et al. (2019), SNe Ib seem to have slightly larger average  $[\text{O I}]/$

[Ca II] ratios than SNe I Ib, still the hypotheses that the SNe I Ib/Ib have the same [O I]/[Ca II] distribution can not be rejected at the significance level  $p > 0.25$ , based on the two-sample Anderson–Darling (AD) test. For SNe Ic, the difference is significant when compared with He-rich objects (SNe I Ib + Ib), with  $p < 0.001$ . Similarly, the [O I]/[Ca II] of SNe Ic-BL is significantly larger than SNe I Ib/Ib ( $p < 0.001$  when compared with both I Ib and Ib), but the distribution is indistinguishable from SNe Ic ( $p \approx 0.23$ ). These findings are consistent with Fang et al. (2019).

From Figure 7(c), a possible [O I] width sequence is also discerned: SNe I Ib → SNe I Ib → SNe Ic → SNe Ic-BL. Unlike the case of [O I]/[Ca II], the differences between SNe I Ib/Ib/Ic are significant, showing an increasing trend ( $p \approx 0.09$  for SNe I Ib versus SNe I Ib and  $p \approx 0.04$  for SNe I Ib versus SNe Ic). While SNe I Ib and SNe Ic are limited to a narrow range, occupying the low and high ends of  $\Delta\lambda_{\text{blue}}$ , respectively, the range of the [O I] width of SNe I Ib is rather large.

In the early-phase spectra, the SNe Ic-BL show evidence of fast-expanding ejecta. The average photospheric velocity of SNe Ic-BL, measured near light-curve peak, is about 20,000 km s<sup>-1</sup>, much larger than that of the canonical SNe (<10,000 km s<sup>-1</sup>; see Lyman et al. 2016). Surprisingly, the [O I] width distribution of SNe Ic-BL is not statistically different from normal SNe Ic. The null hypothesis can be rejected only at the significance level  $p \approx 0.21$  from the AD test when compared with SNe Ic. The AD significance level  $p$  reduces to 0.012 when the [O I] width distribution of SNe Ic-BL is compared with the canonical SNe (I Ib + Ib + Ic). If the [O I] width is transformed to velocity as

$$\frac{v}{c} = \frac{\Delta\lambda}{6300 \text{ \AA}}, \quad (3)$$

the average velocity of SNe Ic-BL is about 3300 km s<sup>-1</sup>, slightly larger than that of the canonical SNe (about 2900 km s<sup>-1</sup>) and SNe Ic (about 3100 km s<sup>-1</sup>). The difference of the velocity scales of the innermost ejecta between SNe Ic-BL and the canonical objects is not as striking as the photospheric velocities around the light-curve peak, which measure the expansion velocities of the outermost ejecta.

For both [O I]/[Ca II] and [O I] width, it is clear from Figures 7(b) and (c) that SNe I Ib/Ib are lower than the average (black dashed line), while SNe Ic and Ic-BL are higher. The above discussions are summarized in Figure 8.

#### 4.2. [O I]/[Ca II]–[O I] Width Correlation

In Figure 7(a), the [O I]/[Ca II] ratio is plotted against the [O I] width for comparison. The objects with small [O I]/[Ca II] tend to have narrow [O I]. The two quantities are moderately correlated (Spearman correlation coefficient  $\rho = 0.51$ ), and the correlation is significant, with  $p < 0.0001$  for the sample size of 103 objects.

To further investigate the dependence of the [O I] width on the [O I]/[Ca II] ratio, in Figure 7, the local nonparametric regression is performed to the full sample (black dashed line). To estimate the uncertainties, we run 10<sup>4</sup> simulations. In each trial, the sample is resampled with replacement, and for each object in the new sample, its [O I]/[Ca II] ratio and the [O I] width are added by the errors, which are assumed to follow Gaussian distribution. Then local nonparametric regression is applied to the new sample. The 97.5% and 2.5% percentages of

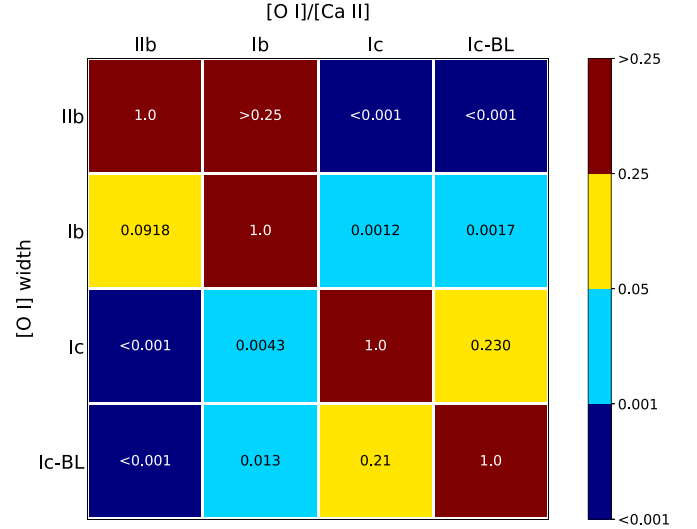


**Figure 8.** Matrix of AD test significance level when the [O I]/[Ca II] and [O I] width distributions of different SN subtypes are compared. The upper-right region is for the [O I]/[Ca II] ratio, and the lower-left region is for the [O I] width  $\Delta\lambda_{\text{blue}}$ . The color bar indicates the probability that the samples are drawn from the same distribution, and the blue end indicates significant differences.

the results from 10<sup>4</sup> simulations are defined to be the boundaries of the 95% CI of the regression, as labeled by the gray shaded region in Figure 7.

The linear regression is performed to the full sample, because analytical form could be useful for further study. The best-fit result gives

$$\log \frac{\Delta\lambda_{\text{blue}}}{\text{\AA}} = (0.16 \pm 0.03) \times \log[\text{O I}]/[\text{Ca II}] + (1.74 \pm 0.01). \quad (4)$$

From the result of local nonparametric regression, the increasing tendency stops at roughly  $\log[\text{O I}]/[\text{Ca II}] = 0.4$  (or  $[\text{O I}]/[\text{Ca II}] = 2.5$ ). If the line regression analysis is restricted to the objects with  $\log[\text{O I}]/[\text{Ca II}] < 0.4$  ( $N = 82$ ), the correlation becomes significant with  $\rho = 0.56$  and  $p < 0.0001$ . For objects with  $\log[\text{O I}]/[\text{Ca II}] < 0.4$ , the best linear regression gives

$$\log \frac{\Delta\lambda_{\text{blue}}}{\text{\AA}} = (0.22 \pm 0.04) \times \log[\text{O I}]/[\text{Ca II}] + (1.74 \pm 0.01), \quad (5)$$

while for the rest ( $\log[\text{O I}]/[\text{Ca II}] > 0.4$ ,  $N = 21$ ),  $\rho$  reduces to  $-0.07$  and  $p < 0.77$ , indicating no correlation exists. For this range,

$$\log \frac{\Delta\lambda_{\text{blue}}}{\text{\AA}} = (-0.02 \pm 0.18) \times \log[\text{O I}]/[\text{Ca II}] + (1.82 \pm 0.09). \quad (6)$$

The significance of the correlation between [O I]/[Ca II] and [O I] width may be affected by SN subtypes and line profile classes as follows:

1. SN sub type: Objects of different SN subtypes (labeled by different colors) behave differently in Figure 9. It is clear that the helium-rich objects (SNe I Ib + Ib) show an increasing tendency ( $\rho = 0.53$ ,  $p < 0.0001$ ). The local nonparametric regression technique is applied to the

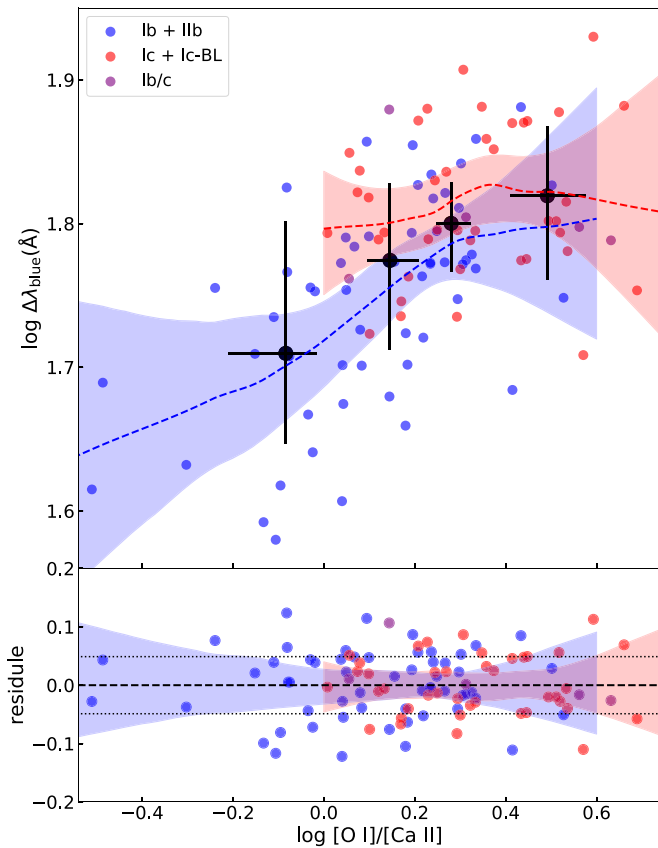


**Figure 9.** Upper panel: the relation between the  $[O\ I]/[Ca\ II]$  ratio and the  $[O\ I]$  width  $\Delta\lambda_{\text{blue}}$ , with SNe of different origins (He star and CO core) labeled by different colors. The 103 objects are divided into five groups ( $\sim 20$  objects in each group) according to the range of the  $[O\ I]/[Ca\ II]$  ratio, and the black dots represent the mean value of each group. The blue dashed line is the result of the local nonparametric regression to helium-rich SNe (Ib + IIb), and the red dashed line is for helium-deficient SNe (Ic + Ic-BL). The shaded regions are the 95% CI (see the main text for details). A clear increasing trend can be discerned. Lower panel: the residual of the fitting. The dotted lines represent the standard deviation of the residual, which is about 0.06 dex ( $\sim 15\%$  in linear scale).

helium-rich SNe, with the same bootstrap-based uncertainties introduced above. The result and the 95% CI are shown by the blue dashed line and the blue shaded region in Figure 9.

However, the  $[O\ I]$  width of the helium-deficient SNe (SNe Ic + Ic-BL) remains (almost) constant as  $[O\ I]/[Ca\ II]$  increases, showing large scatter, and no correlation can be discerned ( $\rho = 0.10$ ,  $p < 0.54$ ). This is consistent with the result of the local nonparametric regression, as shown by the red dashed line and the red shaded region (95% CI) in Figure 9.

- Line profile: The  $[O\ I]/[Ca\ II]$ - $[O\ I]$  width correlation separately shown for different line-profile classes is plotted in Figure 10. The NC objects have the tightest correlation ( $\rho = 0.60$  with  $p < 0.0006$ ), followed by DP and AS ( $\rho = 0.58$  and  $0.54$ , with  $p < 0.0238$  and  $0.0005$ , respectively). For GS objects, the correlation is weak and not significant ( $\rho = 0.34$  with  $p < 0.1297$ ).

The above discussions are summarized in Table 3.

Spectral phase is also a possible factor that affects the correlation, as both  $[O\ I]/[Ca\ II]$  and  $\Delta\lambda_{\text{blue}}$  are time dependent, although not sensitive (Maurer et al. 2010; Fang et al.

2019). In Section 6.1, the effect of spectral evolution will be discussed.

#### 4.3. $[O\ I]/[Ca\ II]$ and Line Profiles

The cumulative fractions of  $[O\ I]/[Ca\ II]$  in terms of the line profiles are shown in the upper panel of Figure 11. The GS objects tend to have the largest  $[O\ I]/[Ca\ II]$  on average, followed by NC/AS, then DP. However, such difference is not significant, possibly except for the difference between DP and GS, where the null hypothesis can be rejected at a significance level  $p \approx 0.08$  from the AD test. The distributions of the AS and NC objects are remarkably similar, and the  $[O\ I]/[Ca\ II]$  distributions of all line profiles are indistinguishable from the average ( $p > 0.25$  from the AD test).

To investigate how the distributions of the line profiles change as the  $[O\ I]/[Ca\ II]$  ratio increases, the full sample is binned into five groups with equal numbers of members ( $N = 20$  or  $21$ ) according to the  $[O\ I]/[Ca\ II]$ . In each group, the fraction of each line profile is calculated. The results are plotted by the colored solid lines in the lower panel of Figure 11.

It is clear that there is a systematic trend where the fraction of GS objects increases as the  $[O\ I]/[Ca\ II]$  ratio increases, and then becomes saturated at  $\log [O\ I]/[Ca\ II] \sim 0.3$  ( $\rho = 0.82$ ,  $p < 0.09$ ). For DP objects, the trend goes to the opposite direction ( $\rho = -0.82$ ,  $p < 0.06$ ). Another interesting feature is the fractions of NC and AS objects are fluctuating around 0.3, and no significant dependence on  $[O\ I]/[Ca\ II]$  can be discerned ( $\rho = -0.41$ ,  $p < 0.49$  for NC and  $\rho = -0.40$ ,  $p < 0.51$  for AS).

## 5. Physical Implications

In Sections 3 and 4, the statistical properties of the  $[O\ I]$  profile, the  $[O\ I]/[Ca\ II]$  ratio, and the  $[O\ I]$  width  $\Delta\lambda_{\text{blue}}$ , along with their mutual relations, were investigated. In this section, the possible physical implications behind the statistics are discussed.

### 5.1. Constraints on the Ejecta Geometry

As introduced in Section 2.4, different ejecta geometry will lead to different line profiles. To further constrain the configuration of the ejecta, it is useful to compare the observational data with some models. For this purpose, a specific bipolar explosion model(s) from Maeda et al. (2006) is employed, as this model has been frequently referred to in previous works to study the ejecta kinematics through the  $[O\ I]$  profile. Note that the model prediction should not be overinterpreted, given various assumptions under which the model is constructed. For example, the models are assumed to be perfectly axisymmetric, and the two hemispheres are symmetric, which are probably too simplified. Indeed, both the consistency and the inconsistency between the data and the model are important; the latter will be useful to clarify which components are still missing in the model, by investigating which assumption is a potential cause of the inconsistency.

To compare the observational data to the theoretical predictions, the multi-Gaussian fit procedure is applied to the synthetic spectra of the bipolar explosion models (Maeda et al. 2006) in the same way as it was applied to the observational data. In this model sequence, oxygen-rich materials are distributed in a torus-like structure surrounding the bipolar jets that convert the stellar material (e.g., oxygen) into the Fe-peak elements (Maeda et al. 2002, 2006, 2008; Maeda & Nomoto 2003). The  $[O\ I]$  profiles of

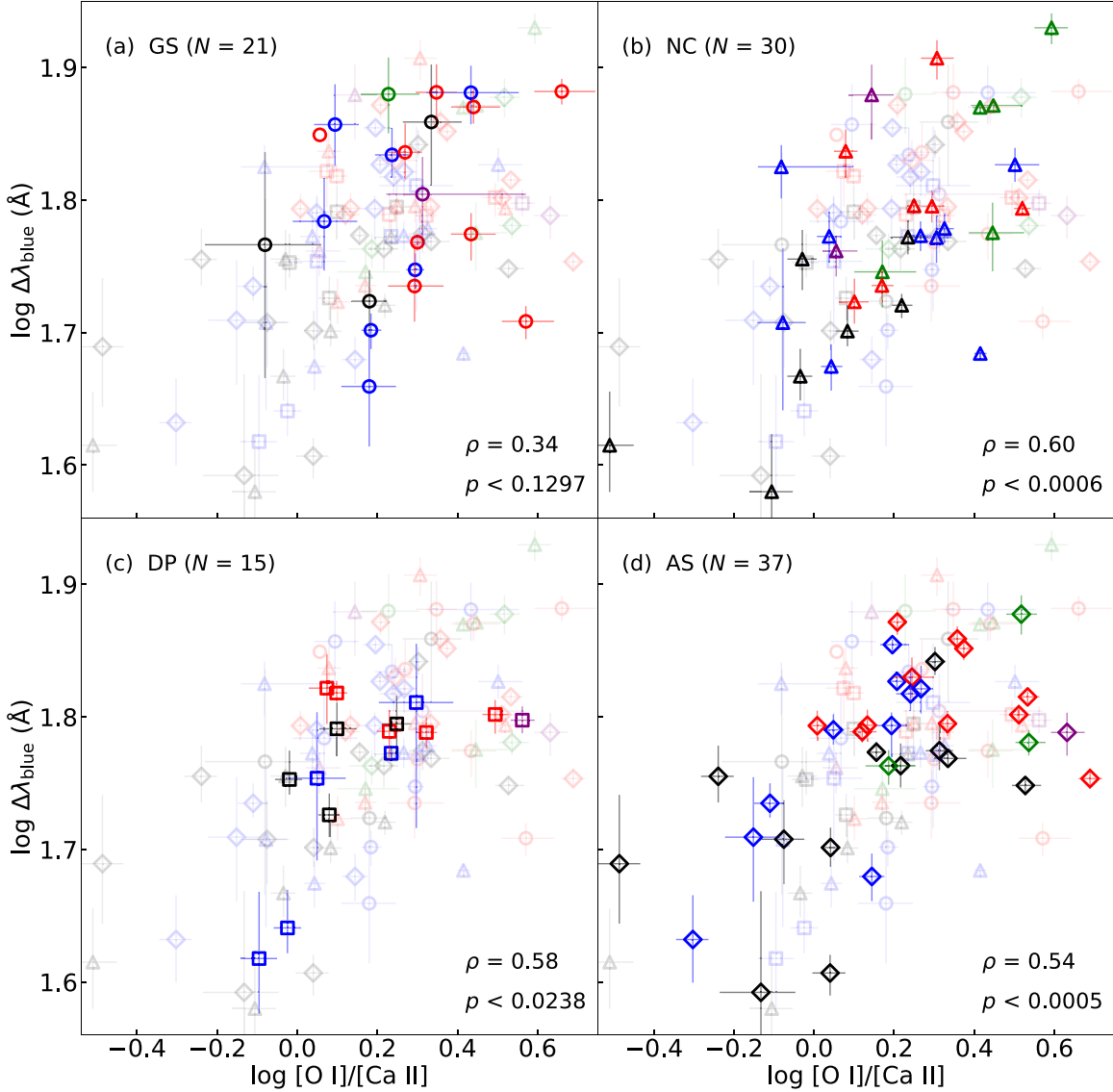


**Figure 10.** The correlations between the [O I]/[Ca II] ratio and [O I] width of different line-profile classes, and the comparison with other line profiles, are plotted in different panels. The meanings of the different colors and markers are the same as in Figure 7. It is clear that NC objects show the tightest correlation, followed by DP and AS. The correlation of GS objects is weak.

the models depend on the degree of asphericity and the viewing angle. In this work, two representative models in Maeda et al. (2006), the mildly aspherical model (BP2) and the extremely aspherical one (BP8), are employed.

A basic assumption of the SN ejecta kinematic is homologous expansion, i.e.,  $v(r, t) = r/t$ , where  $v(r, t)$  is the velocity of the point located at radial coordinate  $r$  at time  $t$ . For a photon emitted from  $\vec{r}$ , the Doppler shift of its wavelength is  $\Delta\lambda = -\lambda_0(v_{\parallel}/c)$ , where  $\lambda_0$  is the intrinsic wavelength and  $v_{\parallel}$  is the line-of-sight velocity toward the observer. For the homologously expanding ejecta,  $\Delta\lambda \propto d$ , where  $d$  is the projection of  $\vec{r}$  onto the direction of the line of sight. At late phases, the photons emitted from the same plane, which is perpendicular to the line of sight, have the same observed wavelength. The line profile therefore provides the “scan” of the integrated emissions on these planes. The readers may refer to Maeda et al. (2008) and Jerkstrand (2017) for more detailed discussions on the formation of the nebular line profile.

For the BP models, the O-rich material is distributed in a torus. When the ejecta is viewed from the edge-on direction, the integrated emission on the scan plane increases as it moves from the outer edge toward the inner edge of the hole, then decreases as it moves further to the center, where the integrated emission reaches its minimum. The [O I] is therefore expected to have a horn-like profile. If the ejecta is viewed from the axial direction, i.e., along the jet, the integrated emission monotonically increases as the scan plane moves toward the center. Most of the O-rich materials are distributed on the equatorial plane, and therefore contribute to the flux at  $v \approx 0 \text{ km s}^{-1}$ , giving rise to the narrow-core [O I] profile.

Applying the same multi-Gaussian fit procedure, the [O I] of the extremely aspherical model (BP8) is classified into the NC and DP profiles if the viewing angles from the jet axis are  $0^\circ$ – $30^\circ$  and  $70^\circ$ – $90^\circ$ , respectively. For the mildly aspherical model (BP2), the corresponding viewing angles change to  $0^\circ$ – $20^\circ$  and  $50^\circ$ – $90^\circ$ . Some examples of the fitting results are shown in Figure 12. If the viewing angles are just randomly distributed

**Table 3**  
Factors Affecting the [O I]/[Ca II]-[O I] Width Correlation

	$\rho$	$p$
log[O I]/[Ca II]		
<0.4	0.56	<0.0001
>0.4	-0.07	0.7706
Line profile		
GS	0.34	0.1297
NC	0.60	0.0006
DP	0.58	0.0238
AS	0.54	0.0005
AS + DP	0.56	<0.0001
GS + NC	0.50	0.0003
SN subtypes		
Iib	0.67	<0.0002
Ib	0.48	0.0064
Iib + Ib	0.58	<0.0001
Ic	0.02	0.8948
Ic-BL	0.56	0.1108
Ic + Ic-BL	0.14	0.3862

without any preference, the fractions of different line profiles can be estimated by

$$f = \frac{1}{2\pi} \int_{\theta_0}^{\theta_1} 2\pi \sin \theta d\theta, \quad (7)$$

where  $\theta_0$  and  $\theta_1$  are the lower and upper limits of the viewing angle described above. The occurrence rates of the DP objects for the bipolar explosion are 34% (BP8) and 68% (BP2). Using the same method, the corresponding NC fractions are 13% and 6%. The results are summarized in Table 4.

It should be noted that the assumption of randomly distributed viewing angle may not be valid for SNe Ic-BL, as these events are frequently accompanied by the occurrence of GRBs and may favor the axial direction. However, the number of these events is small in this sample ( $N = 9$  out of 103). The following analysis will be restricted to the canonical SESNe (SNe Ic-BL excluded), and SNe Ic-BL will be discussed separately.

The line profile fractions of canonical SESNe are: 21% (GS), 27% (NC), 16% (DP), and 36% (AS). Based on the bipolar explosion models, the observed fraction of DP objects suggests that the fraction of the bipolar supernovae is  $\sim 25\%$  (BP2) to 48% (BP8), if the sample is assumed to be unbiased in orientation and all of the DP objects are originated from the oxygen-rich torus viewed from the edge-on direction. The relatively low fraction of bipolar supernovae also implies that most of the NC objects can not be interpreted by the same configuration but viewed axially. Using the estimated occurrence rates of the NC objects (6% and 13% for BP2 and BP8), the expected NC fraction arising from this configuration is only about 1.5% (BP2) to 6.2% (BP8) of the full canonical SESNe sample, much less than the observed NC fraction (27%). Therefore more than  $\sim 80\%$  of the NC objects can not be interpreted by the bipolar explosion. This may leave a massive oxygen blob moving perpendicular to the line of sight or the enhanced core density as more plausible scenarios.

However, as stated above, the model should not be overinterpreted. The classification of the model [O I] profiles

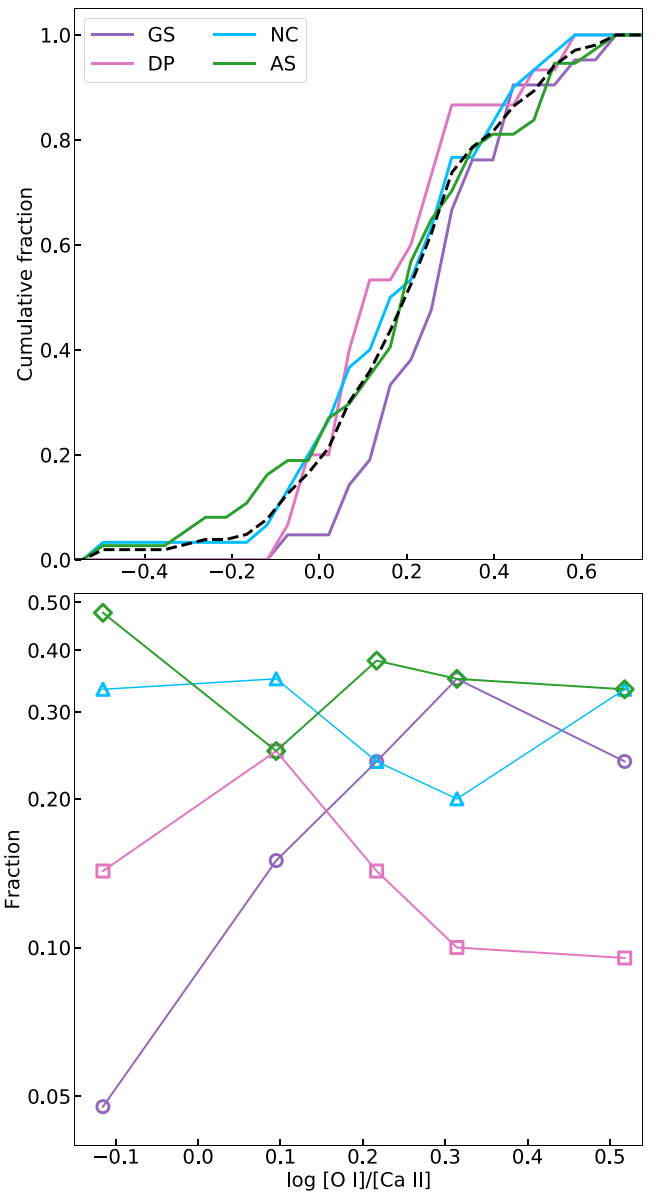


**Figure 11.** Upper panel: the cumulative fractions of  $\log[\text{O I}]/[\text{Ca II}]$  of the objects with different line profiles. The black dashed line is the distribution of the full sample. Lower panel: the fractions of line profile as functions of  $\log[\text{O I}]/[\text{Ca II}]$  are plotted by different colored solid lines and different markers.

into the NC and GS categories is one issue; this is very sensitive to the detailed density distribution, which might be affected by the details of the model construction (e.g., the treatment of the boundary condition in the explosion model). Conservatively, we may thus consider a combination of the NC and GS profiles as the “single-peak” category. If we allow this combined classification, then the single-peak fraction expected in the model is 36% (BP2) to 66% (BP8). Taking into account the fraction of the bipolar model as constrained by the BP fraction (i.e., 26% in BP2 or 50% in BP8), the expected fraction of the single-peak objects is  $\sim 9.4\%$  (BP2) or 33% (BP8). The fraction of the single-peak objects in the canonical SESNe sample is 48%, and thus the bipolar configuration can explain up to 70% of the NC/GS objects in this case.

Another issue is the classification of the AS and DP profiles as individual classes, for the following two reasons: (1) the

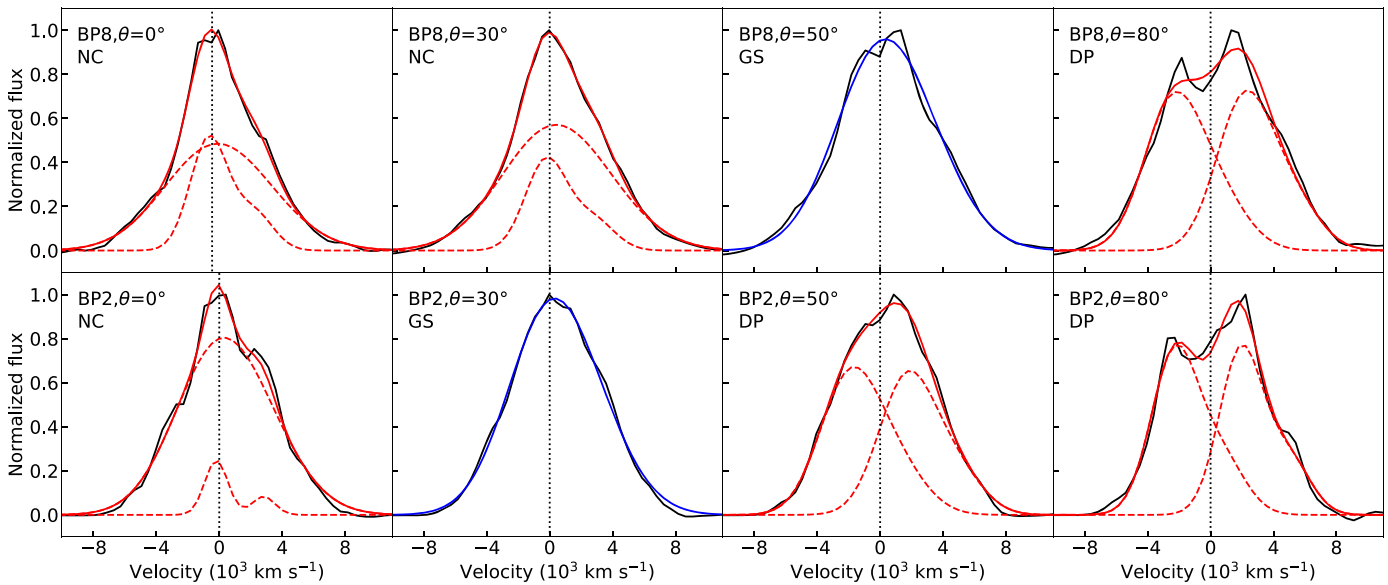


**Figure 12.** The fitting results of the bipolar explosion models with different degrees of axisymmetry and different viewing angles from the direction of the poles. The black solid lines are the model spectra. The blue and red solid lines are the results of one-component and two-component fits. The red dashed lines are the corresponding components. The spectra are plotted in velocity space. The dotted vertical lines represent zero velocity (6300 Å).

**Table 4**  
Properties of the BP2 and BP8 Models

		BP2	BP8
NC	Angle <sup>a</sup>	$\leq 20^\circ$	$\leq 30^\circ$
	Fraction	0.06	0.13
	Scatter of [O I] width	0.003	0.004
GS	Angle	$30^\circ \dots 40^\circ$	$40^\circ \dots 60^\circ$
	Fraction	0.30	0.53
	Scatter of [O I] width	0.050	0.014
DP	Angle	$50^\circ \leq$	$70^\circ \leq$
	Fraction	0.64	0.34
	Scatter of [O I] width	0.012	0.004

**Note.**

<sup>a</sup> The dividing angles for DP objects of BP2 and BP8 models are different from those in Maeda et al. (2008). This is because we employ a different definition of DP in this work, which is based on the fitting procedure described in Section 2. To avoid confusion, throughout the paper, we will adhere to this criterion.

classification of the AS and DP objects in the fitting procedure is not very strict, and for some objects, the classification is found to be interchangeable (see Section 6.3 for further discussion). (2) There is indeed no “AS” profile predicted in the model, and this stems from the two strong assumptions in the model; perfect axisymmetry plus symmetry in the two hemispheres, from which only the line profile symmetric with respect to the line rest wavelength is predicted. In reality, these two assumptions are probably too strong; for example, the observed neutron star kick naturally indicates there must be some overall shift in the momentum distribution within the ejecta (Holland-Ashford et al. 2017; Katsuda et al. 2018). Therefore, we may consider the AS and DP collectively as the “non-single profile” category and compare it to the model DP fraction. As combined with the above caveat on the classification between the NC and GS categories, we may then compare the fractions of the “single-peaked category” (NC and GS) and

the “non-single profile” category (AS and DP). Then, the observed fraction of the non-single profile category is 52%, while this is 64% (BP2) or 34% (BP8). The single-peak category accounts for 48% of the canonical SESNe sample, and its fraction is 34% (BP2) or 66% (BP8). Therefore, the bipolar-like model could account for the full canonical SESNe sample, once one allows the deviation from either the axisymmetry or the symmetry between the two hemispheres to some extent. In other words, the above analysis suggests that (1) the deviation from spherical symmetry could be a common feature in the SN explosion, (2) most of the SN explosion would also have a specific direction, and (3) the configuration having negligible deviation from the axisymmetry and the two-hemisphere symmetry could account for only up to one-third of the canonical SESNe.

The leading scenario for GRBs includes two components: a narrow and relativistic jet for a high-energy GRB emission and a quasi-spherical (but perhaps with a substantial asphericity) component for an optical SN emission. For those associated with GRBs, there could indeed be a preferential viewing direction (Maeda et al. 2006). In the sample of nine SNe Ic-BL, two are definitely associated with GRBs (SNe 1998bw and 2006aj). SN 1997ef might also have been associated with a GRB, and there could also be a bias in the viewing direction for SN 2012ap given its strong radio emission. Therefore, up to  $\sim 45\%$  of the SNe Ic-BL in this sample may indeed suffer from an observational bias in the viewing direction. If we would take this fraction in the model prediction (Table 4), then the NC, GS, and DP fractions expected in the model would change to (as the most extreme case) 48%:17%:35% (BP2) or 52%:29%:19% (BP8). This is indeed compatible with the observed fractions of the NC (56%) and GS (11%) objects, or the sum of the NC and GS fractions (67%; see above for the uncertainty associated with the NC/GS classifications) among the SN Ic-BL sample.

While the specific model used here would not allow for quantitative discussion on the difference between the NC and GS categories (see above), qualitative comparison between

different SN subtypes may still be possible; a larger degree of asphericity leads to a larger ratio of the NC objects to the GS object. This may partly explain a larger fraction of the NC objects in SNe Ic-BL than the other subtypes, together with the effect of a possible bias in the viewing direction as stated above. A lack of the DP objects in SNe Ic-BL is puzzling.<sup>15</sup> As one possibility, this may indicate that SNe Ic-BL may tend to have a specific direction in the explosion, and the deviation from the axisymmetry and/or two-hemisphere symmetry is more important than in the other SESN subtypes. This might be further related to the larger asphericity indicated by a large fraction of the NC objects in SNe Ic-BL. Further investigation focusing on the difference of nebular behaviors between SNe Ic-BL with and without GRB association, based on a larger sample, is required.

### 5.2. [O I]/[Ca II]–[O I] Width Correlation

In Section 4.2, using the thus far largest spectral sample of nebular SESNe, a correlation between the [O I]/[Ca II] ratio and the [O I] width is discerned. In the computed nebular spectra of SESNe, the [O I]/[Ca II] ratio is found to be positively correlated with the progenitor CO core mass (Fransson & Chevalier 1989; Jerkstrand et al. 2015; Dessart et al. 2021), and is therefore routinely employed as the indicator of this very important quantity (Kuncarayakti et al. 2015; Maeda et al. 2015; Fang et al. 2019). Based on this *assumption* (its validity will be discussed in Section 5.4), the correlation implies that the ejecta of SN with a larger CO core tend to expand faster. The typical velocity of the ejecta can be estimated as

$$v^2 \sim \frac{E_K}{M_{\text{ejecta}}} = \frac{E_K}{M_{\text{pre-SN}} - M_{\text{NS}}}. \quad (8)$$

Within each subtype, a more massive progenitor will thus tend to have a larger ejecta mass. If the kinetic energy of the ejecta is a constant, for example,  $10^{51}$  erg, the velocity of the ejecta would be expected to be anticorrelated with the progenitor ZAMS mass or the CO core mass, which contradicts the result in this work. The positive correlation of the [O I] width and [O I]/[Ca II] ratio implies that the SN with a progenitor possessing a more massive CO core will tend to have a larger kinetic energy. Assuming that the kinetic energy is a function of the CO core mass, i.e.,  $E_K = E_K(M_{\text{CO}})$ , the observational tendency in this work can be qualitatively reproduced.

For SNe Ic/Ic-BL, the typical velocity can be estimated as

$$v^2 \sim \frac{E_K}{M_{\text{ejecta}}} = \frac{E_K(M_{\text{CO}})}{M_{\text{ejecta}}} \approx \frac{E_K(M_{\text{O}})}{M_{\text{O}}}, \quad (9)$$

where  $M_{\text{CO}}$  is the CO core mass and  $M_{\text{O}}$  is the mass of the oxygen in the ejecta. Since  $M_{\text{O}}$  is tightly correlated with  $M_{\text{CO}}$ ,  $E_K(M_{\text{CO}})$  can also be written as  $E_K(M_{\text{O}})$ . We assume  $M_{\text{ejecta}} \approx M_{\text{O}}$ , as the oxygen-rich material makes up a significant part of the ejecta of SNe Ic/Ic-BL. If the dependence of  $E_K$  on  $M_{\text{O}}$  is in the form of a power law, i.e.,  $E_K \propto M_{\text{O}}^\alpha$ , and the power index  $\alpha$  is close to unity, the typical velocity of SNe Ic/Ic-BL will be a constant.

For SNe IIB/Ib, if the residual hydrogen envelope of SNe IIB is neglected ( $\sim 0.1 M_{\odot}$ ), Equation (9) becomes

$$v^2 \sim \frac{E_K(M_{\text{O}})}{M_{\text{O}} + M_{\text{He}}} = \frac{E_K(M_{\text{O}})}{M_{\text{O}}} \frac{1}{1 + \frac{M_{\text{He}}}{M_{\text{O}}}}, \quad (10)$$

where  $M_{\text{He}}$  is the mass of the helium in the ejecta. The quantity  $M_{\text{He}}/M_{\text{O}}$  is a decreasing function of CO core mass, as the He burning is efficient for large  $M_{\text{ZAMS}}$  (Dessart et al. 2020). Therefore, the typical velocity of SNe IIB/Ib is an increasing function of  $M_{\text{CO}}$  if  $\alpha \sim 1$ , which explains the behaviors of SNe IIB/Ib in Figure 9.

The gravitational binding energy of a pre-SN progenitor is  $E_g \sim M^2/R$ , where  $M$  is its mass and  $R$  is the radius. The above qualitative analysis gives  $E_K \propto M_{\text{O}}$ . Based on the helium star models in Dessart et al. (2020; the parameters are listed in their Table 1), we derive the scaling relation  $E_K \propto E_g^{0.60}$  to explain the observed correlation. However, the above discussion is greatly simplified, and highly dependent on the stellar evolution and the mass-loss scheme. A more detailed treatment of the quantitative relation between the kinetic energy and the progenitor CO core mass will be presented in a forthcoming work (Q. Fang et al. 2022, in preparation).

Another interesting feature is the dependence of the correlation on the line profile. In Figure 10, if only NC objects are included, the [O I]/[Ca II] ratio and the [O I] width have the tightest correlation, followed by AS and DP objects. If the NC objects originate from the oxygen-rich torus viewed from the axial direction, then the difference in the velocity projection can be neglected, because the viewing angle is restricted to a small range. The effect of the viewing angle can thus be a potential origin of the relatively large scatter seen in GS objects.

To test how the viewing angle affects the scatter level, the same [O I] width measurement is applied to the BP2 and BP8 model spectra. As shown in Section 5.1, the range of the viewing angle relative to the jet-on direction will affect the emission line profile. We measure the [O I] width of the models, and calculate the standard deviation in each line profile group. The results are summarized in Table 4. In general, the scatter levels of the models are much smaller than observation (about 0.06 dex; see the lower panel of Figure 9), but both the BP2 and BP8 models give the correct tendency. The scatter levels of the NC and DP types are relatively small compared with the GS type, as the viewing angles of the NC and DP models are restricted to a narrow range where the effect of velocity projection can be neglected.

### 5.3. [O I]/[Ca II]–Line Profile Correlation

The relation between the [O I]/[Ca II] ratio and the line profiles (Section 4.3) can be summarized as follows: (1) the GS objects have the largest average [O I]/[Ca II], followed by AS/NC, then DP; (2) the fraction of GS objects increases with [O I]/[Ca II]; (3) the fraction of DP objects decreases with [O I]/[Ca II]; and (4) the fractions of NC and AS objects are not monotonic functions of [O I]/[Ca II].

The relation between the [O I] profile distribution and the [O I]/[Ca II] ratio suggests the geometry of the O-rich ejecta probed by the [O I] profile is a function of the progenitor CO core mass, which is *assumed* to be measured by the [O I]/[Ca II] ratio. The interpretation of this relation is uncertain. In the classification scheme of Taubenberger et al. (2009), the

<sup>15</sup> SN 2003jd is a prototype of the DP object (Mazzali et al. 2005; Taubenberger et al. 2009). However, its publicly available spectra do not meet the wavelength range required in this work, so it is not included in our sample.

geometry origins of GS/NC/AS objects are degenerated. Meanwhile, the DP objects are unambiguously related to the O-rich torus, and therefore can be a useful indicator of bipolar explosion. However, the fraction of DP objects is affected by two factors, i.e., the occurrence rate and the (average) degree of asymmetry of the bipolar explosion. Two extreme cases will be discussed in the following, which account for the effects of (A) the bipolar explosion rate and (B) the degree of asymmetry on the interpretation of the  $[\text{O I}]/[\text{Ca II}]-[\text{O I}]$  profile relation.

1. Case A. The global geometry of the ejecta is assumed to be either spherically symmetric (a broad GS base, possibly plus a moving blob to account for the AS and NC objects) or have an axisymmetric bipolar configuration with the *fixed* degree of asymmetry. In this case, the fraction of the DP objects can be an indicator of the occurrence rate of the bipolar explosion. The decreasing trend of the DP fraction in Figure 11 implies the rate of this configuration is anticorrelated with the progenitor CO core mass. Therefore, the ejecta of SESN with a more massive progenitor will tend to be spherically symmetric. This is also consistent with the increasing trend of the GS fraction.

By assuming no spatial preference in the viewing angle, only a small fraction of NC objects originate from the bipolar explosion model viewed from the jet-on direction. The NC/AS objects are characterized by globally spherical symmetry plus a narrow component, which can be interpreted as the massive moving blob or enhanced core density. The insensitivity of the fractions of the AS/NC objects on the  $[\text{O I}]/[\text{Ca II}]$  suggests that the CO core mass is not responsible for the occurrence of these local clumpy structures.

2. Case B. The SESNe in this sample are all assumed to be originated from bipolar explosions (i.e., the occurrence rate is fixed to be 100%) with different degrees of asymmetry, which are reflected by the fractions of the DP objects (Table 4). The bipolar explosions are allowed to be nonaxisymmetric to account for the AS objects (see the discussion in Section 5.1). As already discussed in Section 5.1, if the GS and NC profiles are combined as a “single-peak profile,” and the AS and DP profiles are combined as a “non-single profile” (the assumption of perfect axisymmetry is discarded), the bipolar explosion models could account for the line profile distribution of the full sample. If this is the case, the dependence of the single-peak/non-single profiles on the  $[\text{O I}]/[\text{Ca II}]$  may provide a important constraint on the development of the bipolar configuration of SNe.

The cumulative fractions of  $\log [\text{O I}]/[\text{Ca II}]$  of the objects with single-peak and non-single profiles are plotted in the upper panel of Figure 13. Although the average  $\log [\text{O I}]/[\text{Ca II}]$  of single-peak objects is slightly larger than that of objects with non-single profiles, the difference is not significant, and the  $[\text{O I}]/[\text{Ca II}]$  distributions are indistinguishable ( $p > 0.25$  based on the two-sample AD test). The relation between the  $[\text{O I}]/[\text{Ca II}]$  ratio and the distribution of line profile is derived using the same method as Section 4.3. As shown in the lower panel of Figure 13, the trends where the fraction of the single-peak objects increases as  $\log [\text{O I}]/[\text{Ca II}]$  increases, while the fraction of their non-single counterparts decreases, can be discerned ( $p = \pm 0.90$ , respectively, and  $\rho < 0.03$ ).

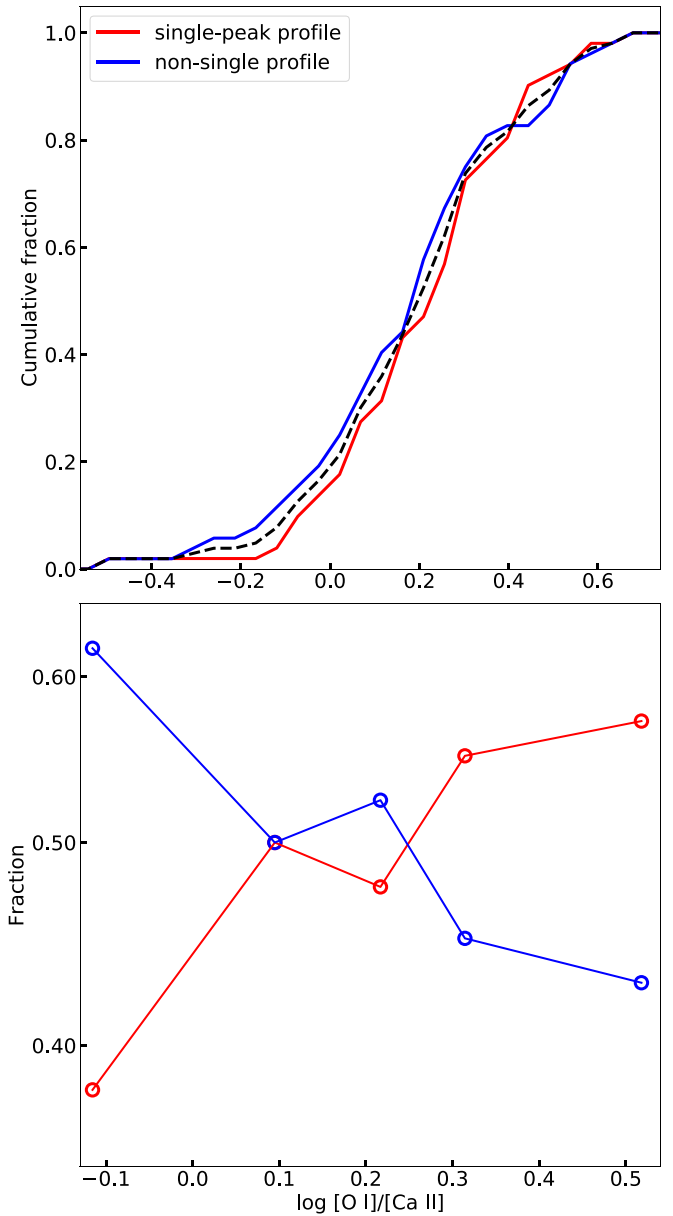


**Figure 13.** Upper panel: the cumulative fractions of  $\log [\text{O I}]/[\text{Ca II}]$  of the objects with single-peak (NC + GS) and non-single (DP + AS) profiles. The black dashed line is the distribution of the full sample. Lower panel: the same as the lower panel of Figure 11 but based on the classification scheme of single-peak and non-single profiles.

The discussion in Section 5.1 shows that the BP2 model has a smaller fraction of single-peak objects than the BP8 model (see Table 4). With  $[\text{O I}]/[\text{Ca II}]$  being a measurement of the CO core mass, the statistics evaluation is qualitatively consistent with the scenario where the ejecta geometry develops as the progenitor CO core mass increases, gradually converting from the mildly aspherical BP2 cases to the extremely aspherical BP8 cases, i.e., the deviation of the explosion from spherical symmetry develops as the CO core mass (or ZAMS mass of the progenitor) increases.

Comparison of the data using the specific bipolar model is just for demonstrative purposes. In reality, the ejecta structure can be more complicated, and the full SESNe samples may not be represented by a single model

sequence, we thus limit ourselves to discuss the general tendency using these specific models.

The investigation on the physics that governs the dependence of the ejecta geometry on the progenitor CO core mass is related to the development of the aspherical explosion, which may put an important constraint on the explosion mechanism of SESNe. However, the interpretation of this dependence can be different (or even opposite) when different assumptions are made, as exemplified by the two extreme cases discussed above. In reality, the situation may be the mixture of the two cases, or even more complicated. To firmly interpret the relation between the [O I]/[Ca II] ratio and the distribution of line profile, we thus need another tool, which should be independent from the [O I] profile, to probe the geometry of the ejecta. The investigation on this topic will be presented in a forthcoming work (Q. Fang et al. 2022, in preparation).

#### 5.4. [O I]/[Ca II] as Measurement of Progenitor $M_{\text{ZAMS}}$

The discussion in Sections 5.2 and 5.3 is largely based on the assumption that the [O I]/[Ca II] ratio is positively correlated with the progenitor CO core mass, and thus its ZAMS mass. This is the case for the currently available models (Fransson & Chevalier 1989; Jerkstrand et al. 2015; Jerkstrand 2017; Dessart et al. 2021). However, whether this diagnostics is robust remains uncertain (Jerkstrand 2017); the [O I]/[Ca II] ratio is affected by the phase of observation, the expansion velocity of the ejecta (or more specifically, kinetic energy), and the distribution of the calcium. In Section 6.1, we will show that the spectral phase will not affect the above correlation. In this subsection, the latter two points, i.e., the effect of kinetic energy, and the pollution of calcium into the O-rich material, are discussed.

1. Kinetic energy. The [Ca II] is emitted from the ash of the explosive burning, the physical properties of which are affected by the explosion energy. The density structure of the ejecta is also related to its expansion velocity, which again affects the [O I]/[Ca II] ratio (Fransson & Chevalier 1989). We will now investigate whether the effect of the explosion energy alone can account for the wide range of the [O I]/[Ca II] ratio.

To simplify the discussion, the amount of the newly synthesized elements, including calcium, is assumed to be positively correlated with the kinetic energy of the ejecta (Woosley et al. 2002; Limongi & Chieffi 2003). With this assumption, for a fixed CO core mass, the kinetic energy will affect the [O I]/[Ca II] in two aspects: (1) SNe with larger kinetic energy will synthesize a larger amount of calcium, which increases the intensity of the [Ca II] and decreases the [O I]/[Ca II] ratio, and (2) with larger kinetic energy, the ejecta will expand faster, which decreases its density and, again, decreases the [O I]/[Ca II] ratio (Fransson & Chevalier 1989).

For the same CO core with different kinetic energy injected, the [O I]/[Ca II] will be expected to be anticorrelated with the expansion velocity of the ejecta, which contradicts the observed correlation in Figure 7. The correlation of the [O I]/[Ca II] ratio and the [O I] width suggests that the effect of the kinetic energy is limited and can not be a main driver of the large range of [O I]/[Ca II] ( $\sim 1$  dex).

2. Calcium pollution. The [Ca II] is mainly emitted by the newly synthesized calcium from the explosive oxygen burning ash (Jerkstrand et al. 2015). However, in several CCSN nebular models, if the calcium produced by the pre-SN nucleosynthesis is microscopically mixed into the O-rich layer through a shell merger (which may happen during the Si burning stage), its contribution to the [Ca II] becomes significant (Dessart et al. 2021). The [O I]/[Ca II] will be dramatically reduced because [Ca II] is a very effective coolant (Dessart & Hillier 2020; Dessart et al. 2021). In this case, [O I]/[Ca II] is no longer a monotonic function of progenitor CO core mass.

Several works (Collins et al. 2018; Dessart & Hillier 2020) reported that the occurrence rate of calcium pollution is high for a more massive star. If the progenitor mass is increased, the [O I]/[Ca II] will be affected by two competing factors along different directions, increased by the CO core mass, but decreased by the higher degree of microscopically mixed calcium. We may consider the most extreme case, in which the effect of the calcium pollution on the progenitor mass is so strong that the correlation between the [O I]/[Ca II] and CO core mass is inverted, i.e., a small [O I]/[Ca II] implies large CO core mass. With this assumption, a constant kinetic energy can produce the correlation between [O I]/[Ca II] and [O I] in Figure 7.

From the current observation, the degree of calcium pollution is difficult to constrain. However, its effect on [O I]/[Ca II] is probably not very strong from several observational lines of evidence. (1) The measured progenitor masses of SNe 2011dh, 2013df, and iPTF 13bvn are relatively small from pre- or post-SN images (Maund et al. 2011; Cao et al. 2013; Van Dyk et al. 2014), and their [O I]/[Ca II] are among the lowest of the full sample. SNe 1998bw and 2002ap are also believed to have massive progenitors; meanwhile, their [O I]/[Ca II] are at the highest end (Nakamura et al. 2001; Mazzali et al. 2002). (2) A correlation between the light-curve width and the [O I]/[Ca II] ratio is reported by Fang et al. (2019). The light-curve width can be an independent measurement of the ejecta mass. If the [O I]/[Ca II] is mainly determined by the degree of microscopic mixing, an anticorrelation between the [O I]/[Ca II] and light-curve width would be expected, which contradicts the observation.

We have discussed the possible factors that would affect the [O I]/[Ca II] ratio. However, it should be emphasized that the current understanding on the [O I]/[Ca II] ratio itself, as well as its relations with the physical properties (CO core mass, kinetic energy, microscopic mixing, etc.) is still limited. To firmly establish the relations between the observables and the ejecta properties, which is crucial to explain the correlation in Figure 7, a sophisticated nebular SESN model with all of the above factors involved is needed.

## 6. Discussion

### 6.1. Temporal Evolution

The nebular spectra in this work cover quite a large range of phases (mean value  $\langle \text{phase} \rangle = 213$  days, standard deviation  $\sigma = 61$  days). Therefore it is important to investigate whether the phases of the spectra will affect the correlation in Figure 7.

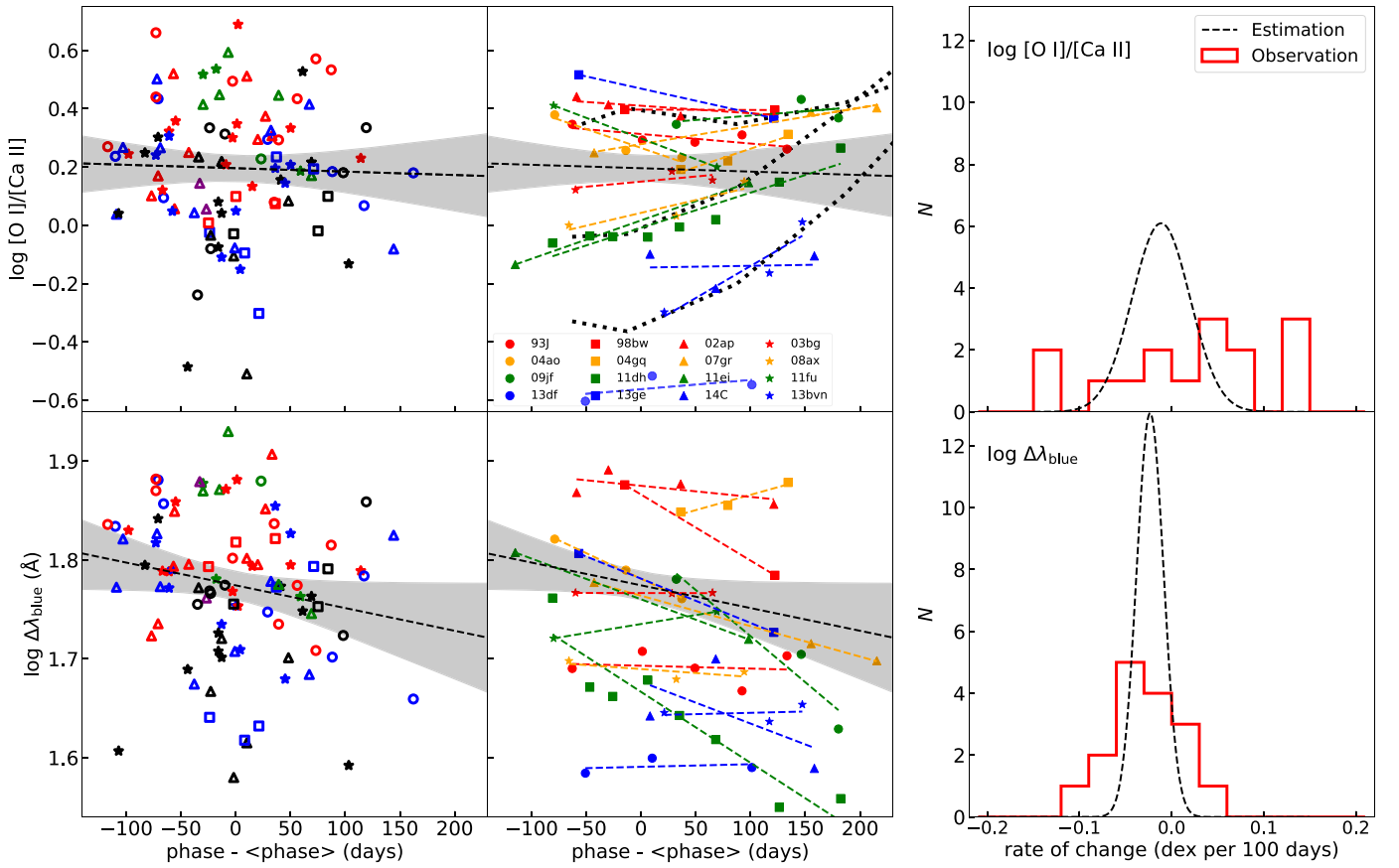


**Figure 14.** Left panels: the  $[O I]/[Ca II]$  ratio and the  $[O I]$  width  $\Delta \lambda_{\text{blue}}$  vs. the spectral phase relative to the mean value of the sample ( $\langle \text{phase} \rangle = 213$  days). The black dashed lines are the results of the linear regression for the full sample, and the shaded regions are the 95% CIs estimated from the bootstrap-based Monte Carlo method. The meanings of the different colors and markers are the same as in Figure 7. Middle panels: the time evolution of  $[O I]/[Ca II]$  and  $\Delta \lambda_{\text{blue}}$  of individual objects. Different objects are labeled by different colors and markers. The color dashed lines are the results of linear regression for each object. The fitting results of the full sample are also plotted for comparison. The black dotted lines in the upper-middle panel are the measurements of the model spectra from Jerkstrand et al. (2015). Right panels: the distributions of the rates of change of  $\log [O I]/[Ca II]$  and  $\log \Delta \lambda_{\text{blue}}$ . The red histograms are the observed rates of change of individual objects. The black dashed lines are the expected distributions of the rates of change estimated from the linear regression of the full sample, scaled to  $N = 16$ . The sources of the spectra are: SN 1993J (Barbon et al. 1995; Matheson et al. 2000; Jerkstrand et al. 2015); SN 1998bw (Patat et al. 2001); SN 2002ap (Foley et al. 2003); SN 2003bg (Hamuy et al. 2009); SN 2004ao (Modjaz et al. 2008; Shivvers et al. 2019); SN 2004gq (Maeda et al. 2008; Modjaz et al. 2014); SN 2007gr Shivvers et al. (2019); SN 2008ax (Chornock et al. 2011; Taubenberger et al. 2011; Modjaz et al. 2014); SN 2009jf (Valenti et al. 2011; Modjaz et al. 2014); SN 2011dh (Shivvers et al. 2013; Ergon et al. 2015); SN 2011ei (Milisavljevic et al. 2013); SN 2011fu (Morales-Garoffolo et al. 2015); SN 2013df (Morales-Garoffolo et al. 2014; Maeda et al. 2015); SN 2013ge (Drout et al. 2016); SN 2014C (Milisavljevic et al. 2015; Shivvers et al. 2019); and iPTF 13bn (Fremling et al. 2016).

The most straightforward method is to calculate the rate of change of the  $[O I]/[Ca II]$  ratio or  $[O I]$  width by following the evolution of each object. However, the number of objects with multiple nebular spectra covering a wide range of phases is too small for such investigation. Fortunately, the main focus of this work is on the statistical properties of these two quantities. Unless there is a strong bias in the sample (for example, objects with large  $[O I]/[Ca II]$  tend to be observed in late phases), the average difference of the quantities at different phases can be employed to estimate the effect of the spectral phase on bulk statistics. In this work, two methods are employed to estimate the rates of change of  $[O I]/[Ca II]$  ratio or  $[O I]$  width; one based on the statistics of the full sample, and the other based on the evolution of individual objects.

The left panels of Figure 14 show the time dependence of the  $[O I]/[Ca II]$  ratio and the  $[O I]$  width  $\Delta \lambda_{\text{blue}}$  of the full sample. In these panels, each data point represents an individual object. The  $\Delta \lambda_{\text{blue}}$  is weakly correlated with the spectral phase ( $\rho = -0.29$ ,  $p < 0.02$ ). The slope from the linear regression is  $-0.023 \pm 0.012$  (unit: dex per 100 days). In the following text, unless explicitly mentioned, the units of rates of change of both

$[O I]/[Ca II]$  and  $[O I]$  width are dex per 100 days). The uncertainty is estimated from  $10^4$  bootstrap resamples, and the 95% CIs are indicated by the shaded regions. If we attribute this phase dependence to the temporal evolution of  $\Delta \lambda_{\text{blue}}$ , on average,  $\Delta \lambda_{\text{blue}}$  changes by about  $-7.7\%$  to  $-2.5\%$  per 100 days, which is in good agreement with the decrease rate reported by Maurer et al. (2010). The same analysis is performed with the  $[O I]/[Ca II]$  ratio, which in turn shows no evidence of temporal evolution ( $\rho = -0.03$ ,  $p < 0.79$ ). Linear regression suggests  $[O I]/[Ca II]$  changes by only  $-0.012 \pm 0.029$  dex (or about  $-9.7\%$ – $4.0\%$  in linear scale) per 100 days.

To examine the evolution of the  $[O I]/[Ca II]$  ratio and the  $[O I]$  width of individual objects, we turn to those SNe in the sample with multiple nebular spectra available from the literature, and the maximum phase span is required to be larger than 100 days. The corresponding measurements of these objects are plotted in the middle panels of Figure 14. The evolution rates are estimated by linear regression. In the SESNE models of Jerkstrand et al. (2015), the oxygen element spreads across a wide range of zones. Initially the  $[O I]$  is dominated by

the emission from the outermost region. As the ejecta expands, the contribution from the innermost region becomes larger, which decreases the average velocity of the emitting elements and therefore the width of the emission line. For most objects ( $N = 12$  out of 16), the [O I] width decreases with time, which is consistent with the above picture. The average and standard deviation of the slopes are  $-0.026 \pm 0.033$ . The distribution of the slopes is also shown in the lower-right panel of Figure 14, with a peak around  $-0.029$ . This is consistent with the slope estimated from the full sample ( $-0.023$ ), and can fully explain the overall time dependence of [O I] width in the lower-left panel of Figure 14.

However, the temporal evolution of [O I]/[Ca II] depends on the physical conditions of the ejecta. The complexity is also discerned in the observational data; the observed slopes of the [O I]/[Ca II] ratio spread over a wide range. The average and standard deviation of the slopes are  $0.027 \pm 0.094$ . Unlike the [O I] width, the distribution of the evolution rates of [O I]/[Ca II] lacks a clear peak, which may possibly explain the lack of correlation between the spectral phase and [O I]/[Ca II]; the different directions of evolution cancel each other out.

It is useful to compare the evolution of [O I]/[Ca II] with theoretical models. For the SNe IIb model spectra of Jerkstrand et al. (2015), the [O I]/[Ca II] increases with time (see also Figure 13 in Jerkstrand 2017). Using the same measurement method in this work, the evolution of the [O I]/[Ca II] of these models is plotted by the black dotted lines in the upper-middle panel of Figure 14 for comparison. The [O I]/[Ca II] and the evolution of the He star model with  $M_{ZAMS} = 12 M_{\odot}$  (M12 hereafter) is consistent with iPTF 13bvn. When compared with SN 2011dh and SN 2008ax, the M13 model evolves faster, but the behaviors are qualitatively similar; the change of [O I]/[Ca II] is mild before  $\sim 300$  days, while at later phases, the slope increases. For M17 model and the objects with large [O I]/[Ca II], the rates of change are approximately negligible before  $\sim 300$  days.

The above discussion motivates the investigation on the possible dependence of the rate of change of [O I]/[Ca II] on [O I]/[Ca II] itself. The He star models of Jerkstrand et al. (2015) and the observational data suggest objects with large [O I]/[Ca II] tend to have slowly evolving [O I]/[Ca II]. For the 16 SNe with wide spectral phase spans and the He star models in Jerkstrand et al. (2015), their [O I]/[Ca II] ratios are corrected to the mean phase (213 days), which are then compared with the slopes estimated from linear regression, as shown in Figure 15. The uncertainties of the corrected [O I]/[Ca II] and the slopes are estimated from the bootstrap-based Monte Carlo method, which includes the uncertainties of the measurement of [O I]/[Ca II] at different phases. An anticorrelation between the slopes and the [O I]/[Ca II] ratios can be discerned ( $\rho = -0.64$ ,  $p < 0.007$ ), especially for objects with  $\log[\text{O I}]/[\text{Ca II}] > 0$ . The relation between the [O I]/[Ca II] and the slope at the low [O I]/[Ca II] end is hard to constrain because only three objects are available (SNe 2013df, 2014C, and iPTF 13bvn) and the scatter is large. The 16 observational data points are then fitted by local nonparametric regression, the result of which is plotted by the black dashed line in Figure 15, and the 95% CI estimated from the bootstrap-based Monte Carlo method is shown by the shaded region.

Limited by the sample size ( $N = 16$ ), the result in this work provides the starting point for the investigation on the dependence of the evolution rate of [O I]/[Ca II] on [O I]/[Ca II]. To firmly establish this relation, we need a larger

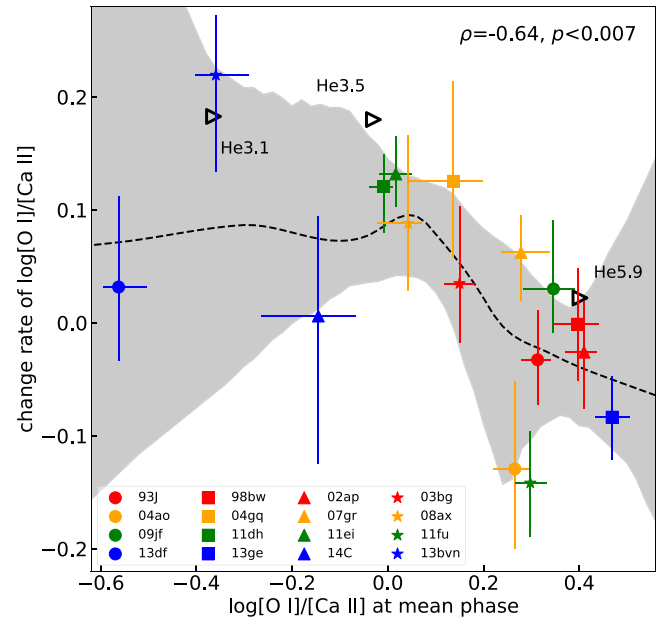


**Figure 15.** The relation between  $\log[\text{O I}]/[\text{Ca II}]$  and its time evolution rate (unit: dex per 100 days). Different objects are labeled by different colors and markers. The SNe IIb model spectra of Jerkstrand et al. (2015) are also plotted for comparison, and the evolution rates of the models are calculated from the measurements at 150–400 days. The dashed line is the result of local nonparametric fit, and the shaded region is the 95% CI estimated from the bootstrap-based Monte Carlo method (see the main text).

sample of SESNe with nebular spectra covering large ranges of phases, especially later than 300 days.

A direct comparison of the nebular spectra at different phases is presented in Figure C1 for some well-observed examples.

To eliminate the effect of spectral evolution, we run  $10^4$  simulations, and in each trial, the rates of change of [O I]/[Ca II] and [O I] width are assigned to each object, which are randomly drawn from (1) the slope estimated from the full sample (the black dashed lines in the right panels of Figure 14), or (2) the distributions of slopes derived from following the evolution of individual objects (the red histograms in the right panels of Figure 14), or (3) the [O I]/[Ca II]-dependent evolution rate (the shaded region in Figure 15). The [O I]/[Ca II] and [O I] width are then corrected to the mean phase. We find that no matter which distributions and combinations are chosen, the two quantities are significantly correlated, with  $\rho$  ranging from 0.50 to 0.54 and  $p < 0.0001$  for all cases. We therefore conclude that the spectral evolution will not significantly affect the correlation in Figure 7.

In Figure 9, the helium-rich SNe behave differently from their helium-deficient counterparts. However, the average phases of the SN subtypes in this work are similar and no statistical difference can be discerned;  $220 \pm 58$  days for SNe IIb,  $203 \pm 80$  days for SNe Ib,  $202 \pm 56$  days for SNe Ic and  $223 \pm 36$  days for SNe Ic-BL. Therefore temporal evolution can not be the main reason for the different behaviors of the different SN subtypes in both Figures 7 and 9, which can be another evidence of the limited effect of the spectral phase on the correlation.

## 6.2. The Effect of Asymmetric $H\alpha/[N II]$

In Section 2, to derive the “clean” [O I] profile, the excess flux at the red wing of [O I] is subtracted by assuming it is

**Table 5**  
Excess Emission Profiles

Geometry	Line Profile	Notes <sup>a</sup>
Thin shell	Flat-top	$dR_{\text{sh}} = 0.2R_{\text{sh}}$
Thick shell	Flat-top	$dR_{\text{sh}} = 0.6R_{\text{sh}}$
Uniform disk	$\sqrt{1 - \left(\frac{\lambda - \lambda_{\text{sym}}}{\Delta\lambda}\right)^2}$	$\Delta\lambda = 220 \text{ \AA}$
Uniform sphere	$1 - \left(\frac{\lambda - \lambda_{\text{sym}}}{\Delta\lambda}\right)^2$	$\Delta\lambda = 220 \text{ \AA}$

**Note.**

<sup>a</sup>  $R_{\text{sh}}$  is the maximum radius of the shell, and  $dR_{\text{sh}}$  is its thickness.

symmetric with respect to 6563 Å. However, this assumption is not necessarily valid and will affect the line width measurement. For example, if the real center of the excess flux is redshifted, assuming a symmetry with respect to 6563 Å will result in oversubtraction of the [O I] and underestimation of the line width. It is not always easy to tell whether such asymmetry exists from the nebular spectra, as the [O I] and the excess flux are always blended. In this subsection, we will quantitatively estimate how the asymmetry of the H $\alpha$ -like structure affect the measurements.

First, an [O I] component, which is composed of two Gaussian functions with the same standard deviation ( $\sigma = 50 \text{ \AA}$ ), is simulated. The central wavelengths are fixed at 6300 and 6364 Å, and the intensity ratio is set to be 3:1 (see Section 2). We then generate a set of excess emissions with detailed profiles listed in Table 5 to account for different distributions of the emitters. The half-width at zero intensity of these profiles is fixed to be 220 Å, based on the  $\sim 10,000 \text{ km s}^{-1}$  outer edge velocity of the excess profile estimated by Maeda et al. (2015). The fluxes of these profiles are set to be 40% of the [O I] emission (about 84% of the full sample). At the same time, we allow the symmetric center  $\lambda_{\text{sym}}$  to move from 6453 to 6673 Å, corresponding to  $|v_{\text{shift}}| \sim 5000 \text{ km s}^{-1}$ .

After adding the [O I] profile by the simulated excess emissions, we repeat the measurement in Section 2, assuming the excess flux is symmetric with respect to 6563 Å. The deviation of the measured line widths ( $\Delta\lambda_{\text{blue}}$ ,  $\Delta\lambda_{\text{red}}$ , and  $\Delta\lambda_{\text{normal}}$ , see Figure 2) from  $\Delta\lambda_{6563}$ , which is defined to be the corresponding measured line widths when the excess emission is symmetric with respect to 6563 Å, is plotted against the symmetric center  $\lambda_{\text{sym}}$  in Figure 16.

It is clear that the asymmetry of the excess flux indeed affects the measured line width. The red width  $\Delta\lambda_{\text{red}}$  is sensitive to the distribution of the emitters and the shift of the symmetric center. If the symmetric center is heavily shifted, or the profile is sharply peaked (i.e., thick shell versus thin shell, or disk versus sphere), the deviation will be large and reach to about 15%–23%. However, the blue width  $\Delta\lambda_{\text{blue}}$  does not show significant deviation in all cases. The deviation of  $\Delta\lambda_{\text{blue}}$  changed by about 5%–8%. Even in the most extreme cases, the deviation will not exceed  $\sim 12\%$  or 0.05 dex, and can not account for the 0.3 dex line width difference reported in this work. Given that  $\Delta\lambda_{\text{blue}}$  is not sensitive to the  $\lambda_{\text{sym}}$  and the spatial distribution of the emitters, in this work,  $\Delta\lambda_{\text{blue}}$  is employed as the measurement of line width.

The excess emission can be attributed to shock-CSM induced H $\alpha$ , radiative powered [N II], or the combination of both (Patat et al. 1995; Jerkstrand et al. 2015; Fang & Maeda 2018). The insensitivity of the  $\Delta\lambda_{\text{blue}}$  to the  $\lambda_{\text{sym}}$  suggests that the identification of the excess emission will make

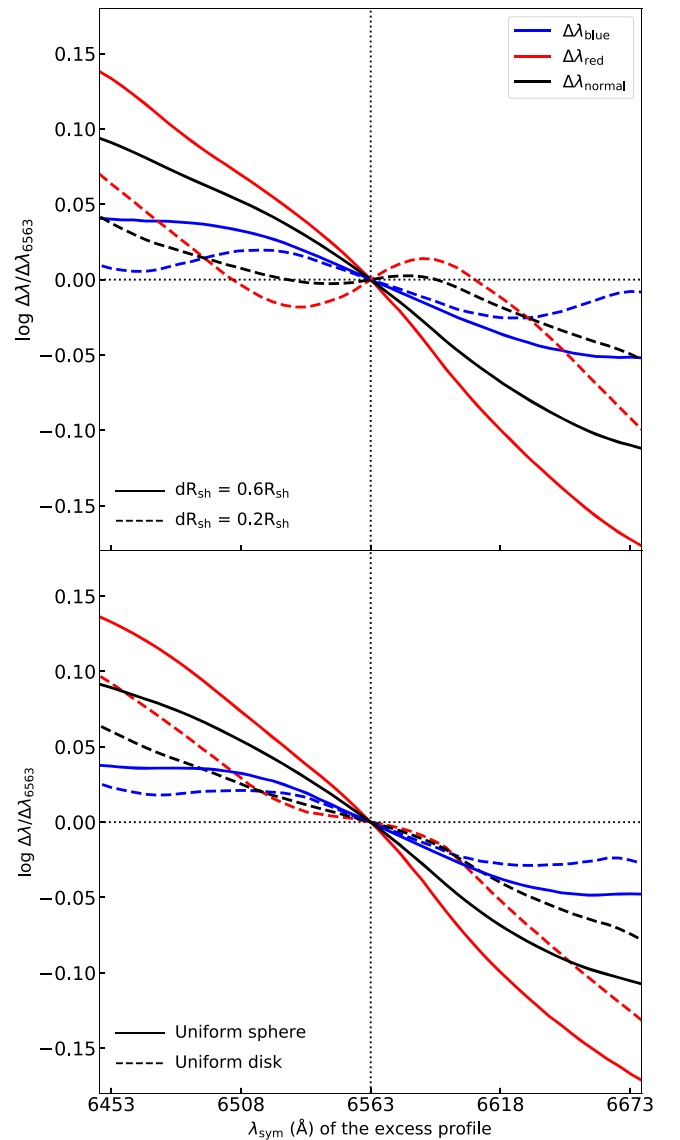


**Figure 16.** The symmetric center of the excess emission and the deviation of the measured line widths from  $\Delta\lambda_{6563}$  (see the main text for definitions).  $\Delta\lambda_{\text{blue}}$ ,  $\Delta\lambda_{\text{red}}$ , and  $\Delta\lambda_{\text{normal}}$  are labeled by different colors, and different distributions of the emitters are labeled by different line styles. In most cases, the  $\Delta\lambda_{\text{blue}}$  is less affected by the asymmetry or the line profile of the H $\alpha$ -like structure, and is therefore selected to be the measurement of the core velocity in this work.

no difference on the measurement. We note that the conditions tested in this subsection are quite extreme, as most objects do not have excess emission as large as  $(\text{H}\alpha \text{ or } [\text{N II}]) / [\text{O I}] = 0.4$  (Fang et al. 2019), and the assumption that  $|v_{\text{shift}}| \sim 5000 \text{ km s}^{-1}$  does not seem realistic. From the very late-phase observation of SN 1993J and SN 2013df, no evidence supports that the boxy profile is significantly asymmetric with respect to H $\alpha$  or [N II] (Maeda et al. 2015), so allowing the central wavelength to move at a velocity as large as  $5000 \text{ km s}^{-1}$  ( $\sim 110 \text{ \AA}$ ) is indeed very conservative.

Observationally, no significant correlation can be discerned between the central wavelength ( $\lambda_c$  in Figure 2) and the [O I] width ( $\rho = 0.12$ ,  $p < 0.21$ ), as would be expected if the difference of the [O I] width was significantly affected by the H $\alpha$ -like structure subtraction, which again supports the argument in this section.

### 6.3. Narrow Core (NC) and Asymmetry (AS): Doppler-shifted Moving Blobs?

As introduced in Section 2.4, the narrow component of the NC profile can be interpreted as a massive oxygen-rich blob moving nearly perpendicular to the line of sight, or enhanced core density. Similarly, the AS profile would require a blob moving with nonnegligible motion in the direction of the line of sight to account for the narrow component. The geometrical origins of NC and AS objects can be unified as ejecta of globally spherical symmetry plus (1) Doppler-shifted moving blobs, or (2) enhanced core density. In the enhanced core density scenario, the narrow component is expected to be centered at its rest wavelength. Further, if the direction of the moving massive blob is isotropic, the amount of the red- and blueshifted narrow components would be similar. In conclusion, the distribution of the narrow component offsets of the AS/NC objects is expected to be symmetric with respect to the Doppler velocity  $|v_{\text{shift}}| = 0 \text{ km s}^{-1}$ . Any deviation from such distribution would require an additional effect beyond geometrical effect.

For the combined sample of NC and AS objects, the shift of the broad base is  $-5.9 \text{ \AA}$ . The standard deviation is  $9.9 \text{ \AA}$ , which is comparable to the resolution  $12.6 \text{ \AA}$  ( $R \sim 500$ ). The low velocity of the broad base is in good agreement with the Gaussian distributed emitter and global spherical symmetry. The histogram of the central wavelength offsets of the narrow component with respect to the broad base are shown in the upper panel of Figure 17. On average, the narrow component is blueshifted ( $-14 \text{ \AA}$ ), which is comparable to its typical width ( $\sim 16 \text{ \AA}$ ), too large for the enhanced core density scenario. The amount of the redshifted objects is only about half of the blueshifted ones ( $N_{\text{red}}/N_{\text{blue}} \sim 0.46$ ). This is also not expected if the narrow core originates from the massive moving blob.

Milisavljevic et al. (2010) already noticed the [O I] with double horns can be classified into two classes: the two horns are symmetric with respect to zero velocity, or one of the horns is located close to  $6300 \text{ \AA}$  and the other one is blueshifted. These two types can both be fitted by a broad base plus a blueshifted narrow component. The result in this work suggests the lack of the redshifted narrow component is a statistically significant phenomenon.

The imbalance of  $N_{\text{blue}}$  and  $N_{\text{red}}$  is mainly driven by the objects with large narrow component offsets. If the analysis is restricted to NC objects, we find  $N_{\text{red}} = 14$  and  $N_{\text{blue}} = 16$ , while for AS objects,  $N_{\text{red}} = 7$  and  $N_{\text{blue}} = 30$ . The above statement is not affected by the boundary of AS/NC. To be specific, the boundary velocity between AS/NC  $v_{\text{boundary}}$ , which is by default  $1000 \text{ km s}^{-1}$ , is allowed to vary from  $500$  to  $3000 \text{ km s}^{-1}$ . The  $N_{\text{red}}/N_{\text{blue}}$  ratio of the NC objects (narrow component offset within  $-v_{\text{boundary}}$  to  $v_{\text{boundary}}$ ) is then calculated. The result is shown as a function of  $v_{\text{boundary}}$  by the blue solid line in Figure 18. When  $v_{\text{boundary}}$  varies from  $500$  to  $1500 \text{ km s}^{-1}$ ,  $N_{\text{red}}/N_{\text{blue}}$  fluctuates between  $0.7$  and  $1.0$ , consistent with the moving blob or enhanced core density scenarios. The ratio of the red- and blueshifted narrow components continues to drop if  $v_{\text{boundary}}$  is larger than about  $1500 \text{ km s}^{-1}$ . This phenomenon suggests the sample especially lacks objects with the narrow component being redshifted by  $\lesssim -1500 \text{ km s}^{-1}$ , or has an unusually enhanced number of objects with narrow components blueshifted by  $\gtrsim +1500 \text{ km s}^{-1}$ . In the following, the possible reasons are discussed.

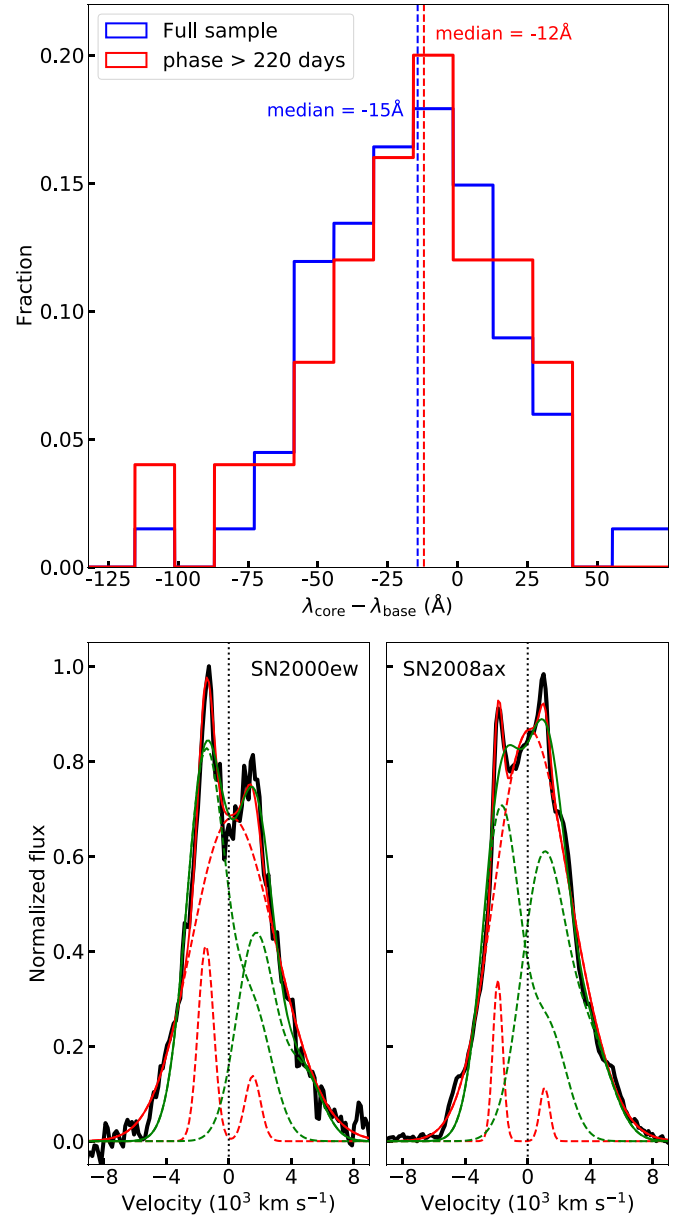


**Figure 17.** Upper panel: the histogram of the central wavelength offset of the narrow core with respect to the broad base. The blue histogram refers to the full NC + AS sample, while the red one is restricted to the objects observed later than 220 days. The dashed lines indicate the median values. Lower panels: alternative fits to the SNe 2000ew and 2008ax. The red solid lines are the results of the two-component fit with an initial guess of case (4), as described in Section 2.4, and the green solid lines are the results where the two components have similar intensity and are forced to blue- and redshifted. The dashed lines are the corresponding components.

(i) *Residual opacity of the inner ejecta.* The imbalance of the red- and blueshifted narrow component can be possibly explained by the radiative transfer effect. Jerkstrand et al. (2015) found the opacity of their He star models is not negligible at around 200 days. For an He star with  $M = 4 M_{\odot}$ , the escape probability of a photon ( $\lambda = 6300 \text{ \AA}$ ) passing through  $3500 \text{ km s}^{-1}$  material is  $\sim 0.85$ . If the photon is emitted from the rear side, it experiences twice the effective opacity. If the inner ejecta is optically thick, the emission from the rear side will be effectively scattered or absorbed, which possibly explains the lack of the redshifted narrow component.

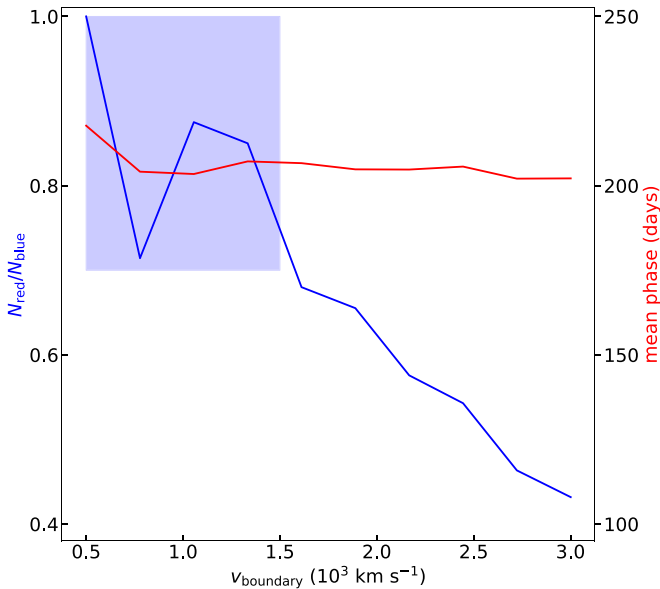


**Figure 18.** The blue solid line shows the relation between the  $N_{\text{red}}/N_{\text{blue}}$  ratio of the NC objects and the  $v_{\text{boundary}}$ , which is defined to be the boundary velocity shift between NC/AS (by default  $1000 \text{ km s}^{-1}$ ). The shaded region indicates the ratio from 0.7 to 1.0. The red solid line shows the relation between the mean phase of the NC objects and  $v_{\text{boundary}}$ , labeled by the right y-axis.

However, this interpretation does not seem realistic for the reasons below: (1) The effect of radiative transfer decreases with the column density, which scales as  $t^{-2}$ , we therefore expect to see more redshifted narrow component at later phases. However, no correlation can be discerned between the narrow component offset and the spectral phase ( $\rho = 0.05$ ,  $p < 0.64$ ). Further, if the analysis is restricted to the objects observed later than 220 days, the imbalance is not eased ( $N_{\text{red}}/N_{\text{blue}} \sim 0.47$ ), and the overall blueshift, which is about  $-12 \text{ \AA}$ , is still too large for the enhanced core density or the moving blob scenarios. In Figure 18, we already find that the  $N_{\text{red}}/N_{\text{blue}}$  of NC objects is a decreasing function of  $v_{\text{boundary}}$ , while no statistical difference can be discerned from the mean phases when  $v_{\text{boundary}}$  varies from 500 to  $3000 \text{ km s}^{-1}$  (red solid line in Figure 18). (2) If the opaque ejecta is scattering-dominated, the peak of the emission will be blueshifted. This effect is usually not very large (see Taubenberger et al. 2009 for some simple models), and can possibly contribute to the small blueshift of the broad base. However, the effect of scattering is not enough to explain the large overall blueshift of the narrow component. (3) The fractional flux of the narrow component,  $\alpha_w$ , can be a rough estimation of the fractional mass of the moving blob. The average value of  $\alpha_w$  is about 0.15. If the effect of self-absorption is included, to absorb the light emitted from such a massive blob, the ejecta will be unrealistically optical thick, resulting in a flux deficit at the redshifted part of the broad base. The line profile will accordingly be heavily distorted, which contradicts the observation.

The relation between  $N_{\text{red}}/N_{\text{blue}}$  of NC objects and  $v_{\text{boundary}}$  in Figure 18 can place an important constraint on the asphericity development of SESNe ejecta. The limited range of  $v_{\text{boundary}}$ , within which  $N_{\text{red}}/N_{\text{blue}}$  is balanced, suggests that the objects with narrow components shifted by  $-1500$  to  $1500 \text{ km s}^{-1}$  can be explained by the moving blob or enhanced core density scenarios. However, the velocity of the blob can not be

too large, otherwise more redshifted narrow components with large velocities would be expected.

(ii) *Misclassification.* Another solution is to use other profiles to fit the AS objects with the extremely blueshifted narrow components. In the lower panels of Figure 17, we take two AS objects, SNe 2000ew and 2008ax, which have narrow component offsets  $< -2000 \text{ km s}^{-1}$ , as examples. The line profile classification in this work is dependent on the initial guess of the fitting, as described in Section 2.4. For these two objects, the initial guess of case (4), i.e., broad base plus a blueshifted narrow component, indeed gives a lower residual than the other cases, and therefore is the *numerical* best fit. However, the initial guess of case (1), i.e., blue- and redshifted components with equal width and intensity, also gives a reasonably good fit, as plotted by the green solid lines in the lower panels of Figure 17.

Taking SNe 2000ew and 2008ax as examples, we are inclined to believe at least some of the AS objects are misclassified, especially those with a trough located at  $\sim 6300 \text{ \AA}$ . The misclassification explains the unusual enhancement of  $N_{\text{blue}}$ . It turns out that, if a fraction of the AS objects are reclassified to DP, the imbalance of the red- and blueshifted narrow components can be eased. However, for a specific object, it is difficult to decide which profile is more appropriate, as both the DP and AS profiles give similarly good fits, while the geometry origins are totally different. The fitting procedure also has an internal shortcoming; each component is assumed to be emitted by the Gaussian distributed emitter, while the intrinsic profile can be much more complicated. This also introduces uncertainty to the geometrical interpretation of the line profile.

## 7. Conclusions

We have conducted a systematic study on the statistical properties of the SESNe nebular spectra. The sample includes 26 SNe Iib, 31 SNe Ib, 32 SNe Ic, 9 SNe Ic-BL, and 5 SNe Ib/c. The investigation involves the morphology of the doublet [O I]  $\lambda\lambda 6300, 6364$ , [O I] width, and the [O I]/[Ca II] ratio. The [O I]  $\lambda\lambda 6300, 6364$  is emitted from the oxygen-rich region, the amount of which is closely related to the properties of the core of the progenitor, especially its mass. Moreover, the [O I] line is also one of the strongest emissions in the nebular spectrum of SESN, and is usually unblended, making it an ideal tracer of the geometry of the O-rich ejecta.

The measurement of the line width is based on the fractional flux of the line, and the result is in good agreement with those estimated in previous works. Although we have discussed the line profile of the [O I], the measurement method of its width applied in this work does not assume any specific profile of the emission, allowing a more general discussion on the velocity scale of the ejecta.

To investigate the geometry of the oxygen-rich ejecta, a multi-Gaussian fitting is applied to the [O I]  $\lambda\lambda 6300, 6363$  of all of the nebular spectra in the sample. The same classification scheme of Taubenberger et al. (2009) is applied, and according to the best-fit parameter, the line profiles are classified as: Gaussian (GS), narrow core (NC; characterized by a Gaussian broad base plus a narrow component with center wavelength  $|v_{\text{shift}}| < 1000 \text{ km s}^{-1}$ ), double-peaked (DP; characterized by a horn-like profile, i.e., blue- and redshifted components with similar widths and intensities), and asymmetry (AS;

characterized by a Gaussian broad base plus a narrow component with center wavelength  $|v_{\text{shift}}| > 1000 \text{ km s}^{-1}$ .

We then conduct a statistical analysis on the [O I] profile, [O I] width, and the [O I]/[Ca II] ratio, along with the mutual relations between these quantities. For convenience, the observational findings are concluded as follows:

1. Although the sample size in this work is about 2.5 times as large as that of Taubenberger et al. (2009), the distributions of the line profile fractions are similar. The similarity between the results of the two samples suggests the sample size is sufficiently large to allow for statistical study.
2. For SNe IIb/Ib/Ic, the distributions of the line profiles are consistent with each other, which indicates the effects of the helium-rich layer and the small amount of the residual hydrogen envelope of SNe IIb are limited. On the other hand, there is a hint (at the  $1\sigma$  level) that the distribution of the line profiles of SNe Ic-BL is different from canonical SESNe (SNe IIb/Ib/Ic).
3. The distributions of the [O I]/[Ca II] ratio of SNe IIb and Ib are similar, but the average ratio for SNe IIb/Ib is significantly smaller than SNe Ic/Ic-BL. This result is consistent with the finding in Fang et al. (2019).
4. The [O I] width shows a similar sequence: it is larger for SNe Ic/Ic-BL than SNe IIb/Ib. The average velocity of SNe Ic-BL, inferred from the line width, is only slightly larger than the canonical SNe. It seems that the velocity of the innermost region is not strongly correlated with the velocity of the outermost ejecta. We leave the systematic investigation on the relation between the velocities measured from the early- and nebular-phase spectra to future works.
5. A significant correlation between the [O I]/[Ca II] ratio and the [O I] width is discerned, where objects with large [O I]/[Ca II] tend to have fast-expanding ejecta. The correlation is dependent on the SN subtypes. For SNe IIb/Ib, the correlation is significant, but can not be discerned for SNe Ic/Ic-BL.
6. The above correlation between the [O I]/[Ca II] ratio and the [O I] width is found to be strong for objects showing a specific line profile. Among the line profile classes, NC objects have the tightest correlation, followed by DP/AS, then GS.
7. The dependence of the line profile on the [O I]/[Ca II] ratio is also observed. The average [O I]/[Ca II] of GS is the largest, followed by AS/NC, then DP objects. By dividing the sample into five groups with an equal number of members and calculating the fractions of the line profiles in each group, we find a steadily increasing tendency for the fraction of GS objects when [O I]/[Ca II] increases, while the fraction of DP objects goes to the opposite direction. Meanwhile, the fractions of NC/AS objects are not monotonic functions of [O I]/[Ca II].

To interpret the observational results, it is crucial to connect the observables to the theoretical models. In this work, we use the [O I]/[Ca II] ratio as the measurement of progenitor CO core mass, as predicted by several nebular SESN models (Fransson & Chevalier 1989; Jerkstrand et al. 2015). The line fitting procedure is applied to the bipolar explosion models of Maeda et al. (2008) to qualitatively constrain the ejecta

geometry. The observational results can be interpreted as follows:

1. For the canonical SNe, the material above the CO core (helium-rich layer and the residual hydrogen envelope) has a limited effect on the ejecta geometry.
2. More than 50% of the objects can not be interpreted by the spherically symmetric ejecta. The deviation from spherical symmetry is commonly seen for all types of SESNe.
3. The fraction of the DP objects is too low for the “strictly” bipolar explosion to be a majority. However, if we discard the condition of perfect axisymmetry and symmetry between the two hemispheres, and further combine the GS and NC profiles as “single-peak” profile and the DP and AS profiles as “non-single” profile, the bipolar explosion can account for the observed line profile fractions of the full sample. If this is the case, the deviation of the observed line profiles from the specific bipolar model sequence can be used to further constrain the nature of the explosion. We conclude that a large fraction of SESNe should have a nonaxisymmetry configuration or imbalance in the two hemispheres to explain the distribution of the line profiles.
4. The progenitors of SNe Ic/Ic-BL have, on average, a more massive CO core than SNe IIb/Ib. The helium-rich layer is most likely stripped by the mass-dependent stellar wind.
5. The correlation between the CO core mass and expansion velocity of the ejecta, inferred from the line width, can not be explained by the constant kinetic energy for different progenitors. In a forthcoming work (Fang et al. 2022, in preparation), we will show that the correlation can be explained by assuming the kinetic energy is tightly correlated with the progenitor CO core mass.
6. Taking the DP profile as an indicator of the nonspherical ejecta, especially those with bipolar configurations, the relation between the [O I]/[Ca II] and DP fraction suggests the ejecta geometry is dependent on the progenitor CO core mass. However, the profile of [O I] itself is not enough to reveal the geometry of the full ejecta. To firmly establish the relation between the progenitor CO core mass and the ejecta geometry, we thus need another probe of the ejecta with bipolar configuration, which should be independent from [O I]. The investigation on this topic will be presented in a forthcoming work (Fang et al. 2022, in preparation).

There remain uncertainties of the theoretical interpretation to the observational relations. (1) Our understanding on the important observable, [O I]/[Ca II], along with its relation with the physical properties (CO core mass, kinetic energy, calcium pollution, etc.), is highly dependent on the current He star model spectra. (2) The line fitting procedure and the classification scheme proposed by Taubenberger et al. (2009) are empirical. The geometrical interpretation of the line profile is complicated by the degeneracy of the fitting, as exemplified by SNe 2000ew and 2008ax; they are originally classified as AS, but the DP profile also provides a reasonably good fit. The inference from the line profile to the ejecta geometry is not straightforward.

To better connect the observation to the properties of the SESNe progenitor, a sophisticated radiative transfer modeling

of the ejecta involving different geometrical configurations, viewing angles, and randomly distributed moving blobs, is required.

The authors would like to thank Takashi Nagao, Luc Dessart, and Tomoya Takiwaki for the very helpful and enlightening discussions. The authors would like to thank the anonymous reviewer for comments that helped to improve the article. Q.F. acknowledges support by Japan Society for the Promotion of Science (JSPS) KAKENHI grant (20J23342). K.M. acknowledges support by JSPS KAKENHI grant (20H00174, 20H04737, 18H05223). M.T. acknowledges support by MEXT/JSPS KAKENHI grant (17H06363, 19H00694, 20H00158, 20H00179). H.K. is funded by the Academy of Finland projects 324504 and 328898.

This research is based (in part) on data collected at Subaru Telescope, which is operated by the National Astronomical

Observatory of Japan. We are honored and grateful for the opportunity of observing the universe from Maunakea, which has cultural, historical, and natural significance in Hawaii.

*Software:* IRAF (Tody 1986, 1993); LACosmic (van Dokkum 2001); SciPy (Virtanen et al. 2020); NumPy (Harris et al. 2020); Astropy (Astropy Collaboration et al. 2013, 2018); Matplotlib (Hunter 2007), R (R Core Team 2021), locfit (Loader 1999, 2018).

## Appendix A Lists of SNe in This Work

In this section, we show the basic properties of the SNeIb (Table A1), Ib (Table A2), Ic (Table A3), Ic-BL (Table A4) and Ib/c (Table A5) in this work.

**Table A1**  
SNe Ib in This Work

SN Name	Host	Date	Phase <sup>a</sup>	Redshift	$E(B - V)^b$	Profile	References <sup>c</sup>
1987K	NGC 4651	1988/02/24	211	0.0027	0.36(+)	NC	F88
1993J	NGC 3031	1993/11/07	203	-0.0001	0.19	AS	M00,J15
1996cb	NGC 3510	1997/07/01	176	0.0030	0.03	AS	Q99
2001ig	NGC 7424	2002/10/08	274	0.0066	0.10	AS	M07a,S09
2003bg	MCG-05-10-15	2003/11/29	254	0.0049	0.02	AS	H09
2006G	NGC 521	2006/06/30	169	0.0171	0.36(+)	AS	This work
2006T	NGC 3054	2006/11/26	284	0.0086	0.08	DP	M07b, M08,M14
2007ay	UGC 4310	2007/11/05	$\gtrsim 190$	0.0147	0.36(+)	GS	This work
2008aq	PGC 43458	2008/06/26	108	0.0075	0.36(+)	AS	M14
2008ax	NGC 4490	2008/11/24	245	0.0019	0.40	AS	T11,M14
2008bo	NGC 6643	2008/10/27	195	0.0053	0.08	AS	S19
2008ie	NGC 1070	2009/10/27	316	0.0136	0.36(+)	AS	This work
2009C	UGC 12433	2009/10/26	297	0.0226	0.36(+)	DP	This work
2009K	NGC 1620	2009/10/26	261	0.0113	0.36(+)	NC	This work
2009ka	Anon	2010/05/06	200	0.0175	0.36(+)	NC	This work
2010as	NGC 6000	2010/08/05	130	0.0078	0.44	DP	F14
2011dh	NGC 5194	2011/12/24	187	0.0020	0.07	NC	S13, E14,E15
2011ei	NGC 6925	2012/06/18	311	0.0089	0.24	GS	M13
2011fu	UGC 1626	2012/07/20	282	0.0185	0.10	AS	MG15
2011hs	IC 5267	2012/06/21	211	0.0057	0.17	NC	B14
2012P	NGC 5806	2012/08/08	197	0.0045	0.29	DP	F16
2012dy	ESO 145-G4	2012/12/23	nebular	0.0103	0.36(+)	AS	Y12
2013ak	ESO 430-G20	2013/09/13	179	0.0035	0.30	NC	Y12
2013bb	NGC 5504	2014/03/02	332	0.0190	0.30	GS	Y12,S19
2013df	NGC 4414	2014/02/04	223	0.0024	0.10	NC	MG14,M15
ASASSN-14az	PGC 110136	2014/11/25	189	0.0067	0.36(+)	AS	S19

### Notes.

<sup>a</sup> Phase relative to the light-curve maximum or discovery date.

<sup>b</sup> Objects labeled by (+) indicate the case where its extinction can not be calculated from the light curve reported by the literature or Na I D absorption. The average  $E(B - V)$  of SN Ib/c (0.36 mag) is adopted for this case.

<sup>c</sup> F88: Filippenko (1988); Q99: Qiu et al. (1999); M00: Matheson et al. (2000); M07a: Maund et al. (2007); M07b: Modjaz (2007); M08: Maeda et al. (2008) H09: Hamuy et al. (2009); S09: Silverman et al. (2009); T11: Taubenberger et al. (2011); Y12: Yaron & Gal-Yam (2012); M13: Milisavljevic et al. (2013); S13: Shivvers et al. (2013); B14: Bufano et al. (2014); E14: Ergon et al. (2014); F14: Folatelli et al. (2014); M14: Modjaz et al. (2014); MG14: Morales-Garoffolo et al. (2014); E15: Ergon et al. (2015); J15: Jerkstrand et al. (2015); M15: Maeda et al. (2015); MG15: Morales-Garoffolo et al. (2015); F16: Fremling et al. (2016); S19: Shivvers et al. (2019).

**Table A2**  
SNe Ib in This Work

SN Name	Host	Date	Phase	Redshift	$E(B - V)$	Profile	References
1985F	NGC 4618	1985/04/01	280	0.0002	0.23	NC	F86
1990I	NGC 4650	1991/04/21	357	0.0097	0.12	NC	E04
1990U	NGC 7479	1991/01/06	189	0.0081	0.52	DP	G94, M01, T09,M14
1997X	NGC 4691	1997/05/13	103	0.0035	0.18	GS	G02,T09
1999dn	NGC 7714	2000/09/01	379	0.0090	0.10	GS	B11
2000ew	NGC 3810	2001/03/17	110	0.0033	0.36(+)	AS	T09
2002dz	MCG-01-01-52	2002/08/10	nebular	0.0184	0.36(+)	DP	S19
2004ao	UGC 10862	2004/11/14	250	0.0059	0.12	DP	E11,S19
2004dk	NGC 6118	2005/05/11	263	0.0052	0.34	AS	M08a, D11, M14,S17
2004gn	NGC 4527	2005/07/06	217	0.0061	0.36(+)	AS	M08b
2004gq	NGC 1832	2005/08/26	249	0.0059	0.25	AS	M08a, M08b, D11,M14
2004gv	NGC 856	2005/08/26	242	0.0200	0.25	GS	M08a, M08b,M14
2005bf	MCG+00-27-05	2005/12/11	213	0.0186	0.14	DP	F06,M14
2006F	NGC 935	2006/06/30	175	0.0139	0.54	NC	G06, M08b,D11
2006ep	NGC 214	2006/12/24	104	0.0152	0.36(+)	NC	This work
2006gi	NGC 3147	2007/02/10	145	0.0094	0.38	NC	T09,E11
2006ld	UGC 348	2007/07/17	258	0.0140	0.36(+)	AS	T09
2007C	NGC 4981	2007/06/20	155	0.0056	0.64	AS	T09, D11,M14
2007Y	NGC 1187	2007/09/22	200	0.0040	0.11	AS(NC)	S09
2007uy	NGC 2770	2008/06/06	141	0.0063	0.79	NC(AS)	R13,M14
2008D	NGC 2770	2008/06/07	140	0.0072	0.65	AS	M09
2008fd	ESO 466-G24	2009/07/23	330	0.0181	0.36(+)	GS	This work
2008im	UGC 2906	2009/08/18	232	0.0090	0.36(+)	GS	This work
2009jf	NGC 7479	2010/06/19	245	0.0068	0.12	NC	S11, V11,M14
2012au	NGC 4790	2012/12/19	284	0.0045	0.06	AS(NC)	M13
iPTF13bvn	NGC 5806	2014/02/21	234	0.0045	0.07	AS(NC)	F16
2014C	NGC 7331	2014/08/25	221	0.0029	0.75	DP	S19
2014ei	MCG-01-13-50	2015/03/27	142	0.0148	0.36(+)	GS	S19
2015Q	NGC 3888	2016/01/07	212	0.0078	0.36(+)	NC	S19
2015ah	UGC 12295	2016/01/07	152	0.0160	0.10	NC	S19
PS15bgt	NGC 6412	2015/12/17	147	0.0090	0.23	GS	S19

**References.** F86: Filippenko & Sargent (1986); G94: Gómez & López (1994); M01: Matheson et al. (2001); G02: Gómez & López (2002); E04: Elmhamdi et al. (2004); F06: Folatelli et al. (2006); G06: Green (2006); M08a: Modjaz et al. (2008); M08b: Maeda et al. (2008); M09: Modjaz et al. (2009); S09: Stritzinger et al. (2009); T09: Taubenberger et al. (2009); B11: Benetti et al. (2011); D11: Drout et al. (2011); E11: Elmhamdi et al. (2011); S11: Sahu et al. (2011); V11: Valenti et al. (2011); M13: Milisavljevic et al. (2013); R13: Roy et al. (2013); M14: Modjaz et al. (2014); F16: Fremling et al. (2016); S17: Shivvers et al. (2017); S19: Shivvers et al. (2019).

**Table A3**  
SNe Ic in This Work

SN Name	Host	Date	Phase	Redshift	$E(B - V)$	Profile	References
1987M	NGC 2715	1988/02/25	157	0.0043	0.45	GS	F90,J91
1990aa	MCG+05-03-16	1991/01/23	140	0.0170	0.36(+)	GS	M01
1991A	IC 2973	1991/04/07	96	0.0105	0.42	GS	M01
1991N	NGC 3310	1992/01/09	$\approx 286$	0.0035	0.12	GS	F91, M01,M08
1994I	NGC 5194	1994/09/02	146	0.0015	0.45	AS	W94, F95, R96,M14
1996aq	NGC 5584	1997/04/02	228	0.0055	0.36(+)	AS	N96,T09
1996D	NGC 1614	1996/09/10	214	0.0149	0.36(+)	GS	D96,T09
1997B	IC 438	1997/09/23	252	0.0095	0.36(+)	GS	T09
1997dq	NGC 3810	1998/05/30	210	0.0033	0.11	DP	N97, M01, T09,M14
2003gf	MCG-04-52-26	2003/11/29	158	0.0087	0.36(+)	AS	S19
2004aw	NGC 3997	2004/11/14	232	0.0159	0.37	NC	T06,M14
2004fe	NGC 132	2005/07/06	240	0.0180	0.32	DP	M08, D11,M14
2004gk	IC 3311	2005/07/10	223	-0.0005	0.47	AS	M08, M14,E11
2004gt	NGC 4038	2005/05/24	152	0.0046	0.10	DP	GY05, T09,M14
2005aj	UGC 2411	2005/08/25	188	0.0085	0.36(+)	AS	This work
2005bj	MCG+03-43-05	2005/08/25	136	0.0222	0.36(+)	NC	This work
2005kl	NGC 4369	2006/06/30	213	0.0034	0.29	DP	M08, M14,D11
2005kz	MCG+08-34-32	2006/06/30	215	0.0278	0.46	AS	F05, M08,D11
2006ck	UGC 8238	2007/01/24	246	0.0245	0.39	NC(AS)	C06, M08,M14

**Table A3**  
(Continued)

SN Name	Host	Date	Phase	Redshift	$E(B - V)$	Profile	References
2007gr	NGC 1058	2008/02/12	170	0.0020	0.09	NC	<a href="#">S19</a>
2007rz	NGC 1590	2008/04/01	115	0.0135	0.36(+)	AS	<a href="#">M14</a>
2008fo	A164012+3943	2009/04/05	240	0.0289	0.36(+)	AS(NC)	This work
2007hb	NGC 819	2008/01/11	140	0.0222	0.36(+)	GS	<a href="#">M14</a>
2008hh	IC 112	2009/08/18	269	0.0196	0.26	GS	This work
2009jy	NGC 3208	2010/05/06	204	0.0103	0.36(+)	AS	This work
2010mb	A160023+3744	2011/03/04	248	0.1325	0.01	NC	<a href="#">B14</a>
2011bm	IC 3918	2012/01/22	263	0.0212	0.06	AS	<a href="#">V12</a>
PTF12gzk	SDSS J221241.53+003042.7	2013/06/10	299	0.0139	0.14	AS	<a href="#">S19</a>
2013ge	NGC 3287	2014/04/28	156	0.0045	0.07	NC	<a href="#">D16</a>
2014L	NGC 4254	2014/06/29	142	0.0078	0.67	NC	<a href="#">Z18,S19</a>
2014eh	NGC 6907	2015/06/16	210	0.0106	0.36(+)	GS	<a href="#">S19</a>
iPTF15dtg	Anon	2016/10/31	327	0.0544	0.06	DP	<a href="#">T16,T19</a>

**References.** F90: Filippenko et al. (1990); F91: Filippenko & Korth (1991); J91: Jeffery et al. (1991); F95: Filippenko et al. (1995); D96: Drissen et al. (1996); N96: Nakano et al. (1996); R96: Richmond et al. (1996); N97: Nakano et al. (1997); M01: Matheson et al. (2001); GY05: Gal-Yam et al. (2005); C06: Colesanti et al. (2006); T06: Taubenberger et al. (2006); M08: Maeda et al. (2008); T09: Taubenberger et al. (2009); D11: Drout et al. (2011); E11: Elmhamdi et al. (2011); V12: Valenti et al. (2012); BA14: Ben-Ami et al. (2014); M14: Modjaz et al. (2014); D16: Drout et al. (2016); T16: Taddia et al. (2016); Z18: Zhang et al. (2018); S19: Shivvers et al. (2019); T19: Taddia et al. (2019); W94: Wheeler et al. (1994); F05: Filippenko et al. (2005).

**Table A4**  
SNe Ic-BL in This Work

SN Name	Host	Date	Phase	Redshift	$E(B - V)$	Profile	References
1997ef	UGC 4107	1998/09/21	282	0.0117	0.00	NC	<a href="#">I00, M00, M01,M14</a>
1998bw	ESO 184-G82	1998/11/26	198	0.0096	0.06	NC	<a href="#">P01, C11,M16</a>
2002ap	NGC 628	2002/08/09	183	0.0021	0.08	NC	<a href="#">F03, Y03,M16</a>
2005nb	UGC 7230	2006/06/30	183	0.0235	0.36(+)	AS	<a href="#">M08, M14,Q06</a>
2006aj	A032139+1652	2006/09/21	206	0.0330	0.15	NC	<a href="#">M06, M14,M16</a>
2007D	UGC 2653	2007/09/18	252	0.0232	0.91	NC	This work, <a href="#">D16</a>
2007I	A115913-0136	2007/07/15	182	0.0215	0.36(+)	AS	<a href="#">B07, T09,M14</a>
PTF10qts	SDSS J164137.53+285820.3	2010/04/27	231	0.0912	0.02	GS	<a href="#">W14</a>
2012ap	NGC 1729	2012/09/23	272	0.0121	0.45	AS	<a href="#">M15</a>

**References.** I00: Iwamoto et al. (2000); M00: Mazzali et al. (2000); M01: Matheson et al. (2001); P01: Patat et al. (2001); F03: Foley et al. (2003); Y03: Yoshii et al. (2003); M06: Modjaz et al. (2006); B07: Blondin et al. (2007); M08: Maeda et al. (2008); T09: Taubenberger et al. (2009); C11: Clocchiatti et al. (2011); M14: Modjaz et al. (2014); M16: Modjaz et al. (2016) W14: Walker et al. (2014); M15: Milisavljevic et al. (2015); D16: Drout et al. (2016); Q06: Quimby et al. (2006).

**Table A5**  
SNe Ib/c in This Work

SN Name	Host	Date	Phase	Redshift	$E(B - V)$	Profile	References
1990W	NGC 6221	1991/02/21	186	0.0042	0.36(+)	NC	<a href="#">T90,T09</a>
1990aj	NGC 1640	1991/03/10	180	0.0053	0.36(+)	NC	<a href="#">M01</a>
1995bb	A001617+1224	1996/01/21	nebular	0.0055	0.36(+)	GS	<a href="#">M14</a>
2005N	NGC 5420	2005/01/22	nebular	0.0163	0.36(+)	AS	<a href="#">H08</a>
2012fh	NGC 3344	2012/11/14	nebular	0.0017	0.36(+)	DP	<a href="#">S19</a>

**References.** M01: Matheson et al. (2001); H08: Harutyunyan et al. (2008); T09: Taubenberger et al. (2009); M14: Modjaz et al. (2014); S19: Shivvers et al. (2019); E90: Evans et al. (1990).

## Appendix B

### Line Fitting Results

In this section, we show the [OI] profile fitting result of SNe IIb (Figure B1), Ib (Figure B2), Ic (Figure B3), Ic-BL and Ib/c (Figure B4).

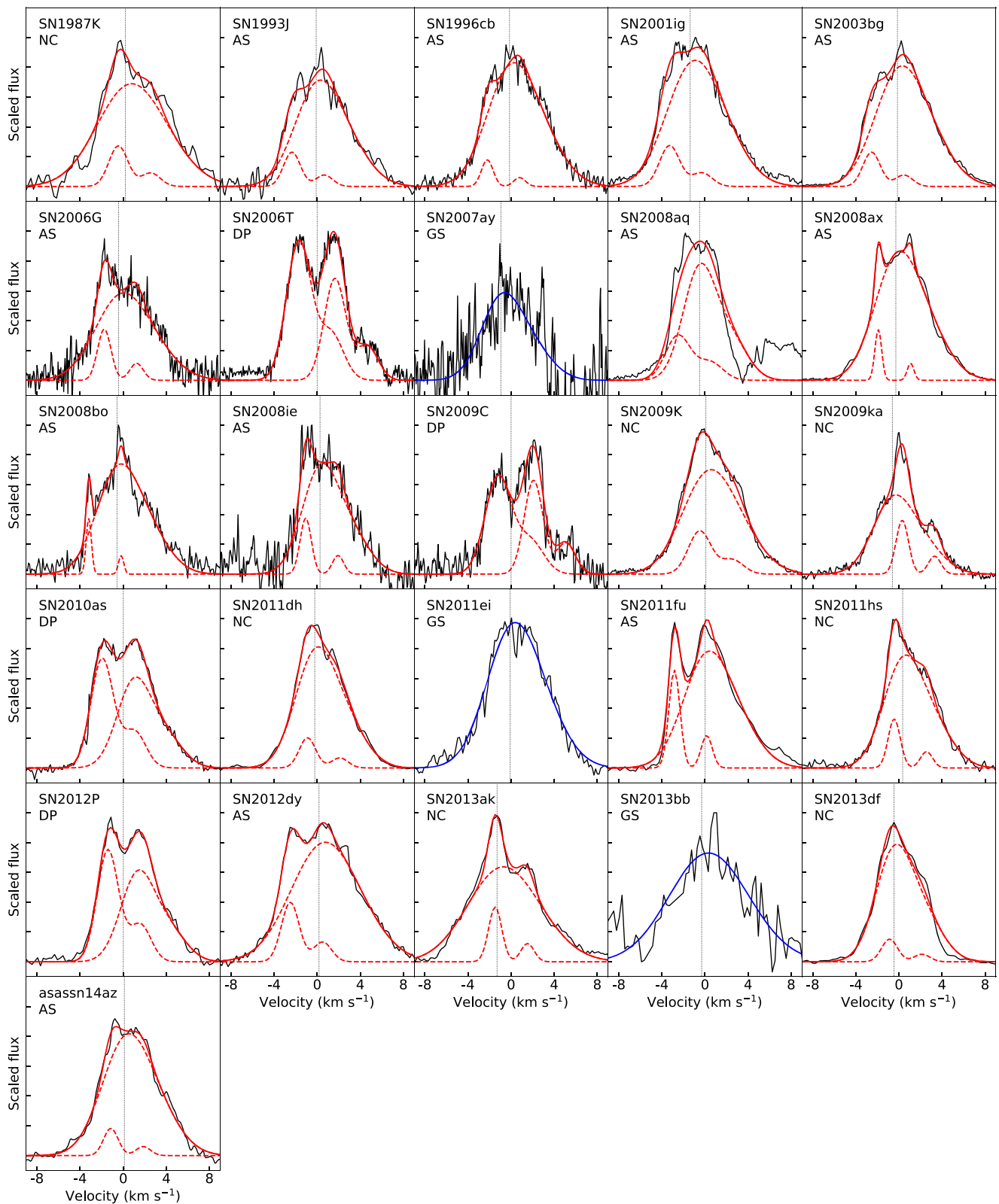


**Figure B1.** Observed [O I] of the SNe IIB in the sample fitted by multi-Gaussians. The spectra (black solid lines) are already subtracted by the background and the symmetric  $H\alpha/[N II]$ . The blue solid lines are the results of a one-component fit. The red solid lines are the results of a two-component fit, and the red dashed lines are the components. The vertical dotted lines are zero velocity (6300 Å) for DP objects or the center wavelength of the Gaussian broad base for GS, NC, or AS objects for reference.

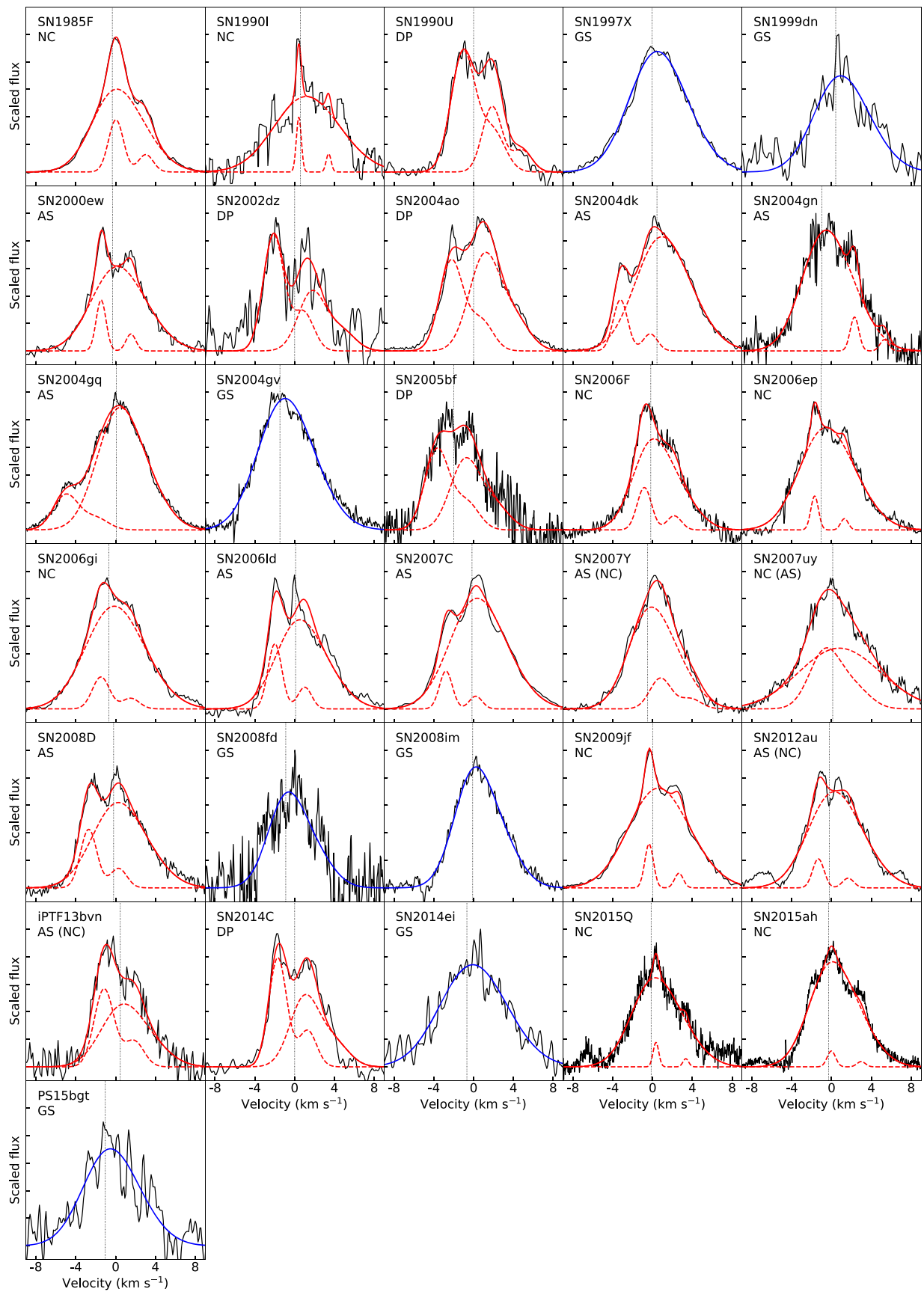


**Figure B2.** Observed [O I] of the SNe Ib in the sample fitted by multi-Gaussians. The spectra (black solid lines) are already subtracted by the background and the symmetric  $H\alpha$ /[N II]. The blue solid lines are the results of a one-component fit. The red solid lines are the results of a two-component fit, and the red dashed lines are the components. The vertical dotted lines are zero velocity ( $6300 \text{ \AA}$ ) for DP objects or the center wavelength of the Gaussian broad base for GS, NC, or AS objects for reference. SN 2005bf is an exception; the [Ca II] of this object is blueshifted by  $\sim 2000 \text{ km s}^{-1}$ , which is then taken as the “center” of SN 2005bf.

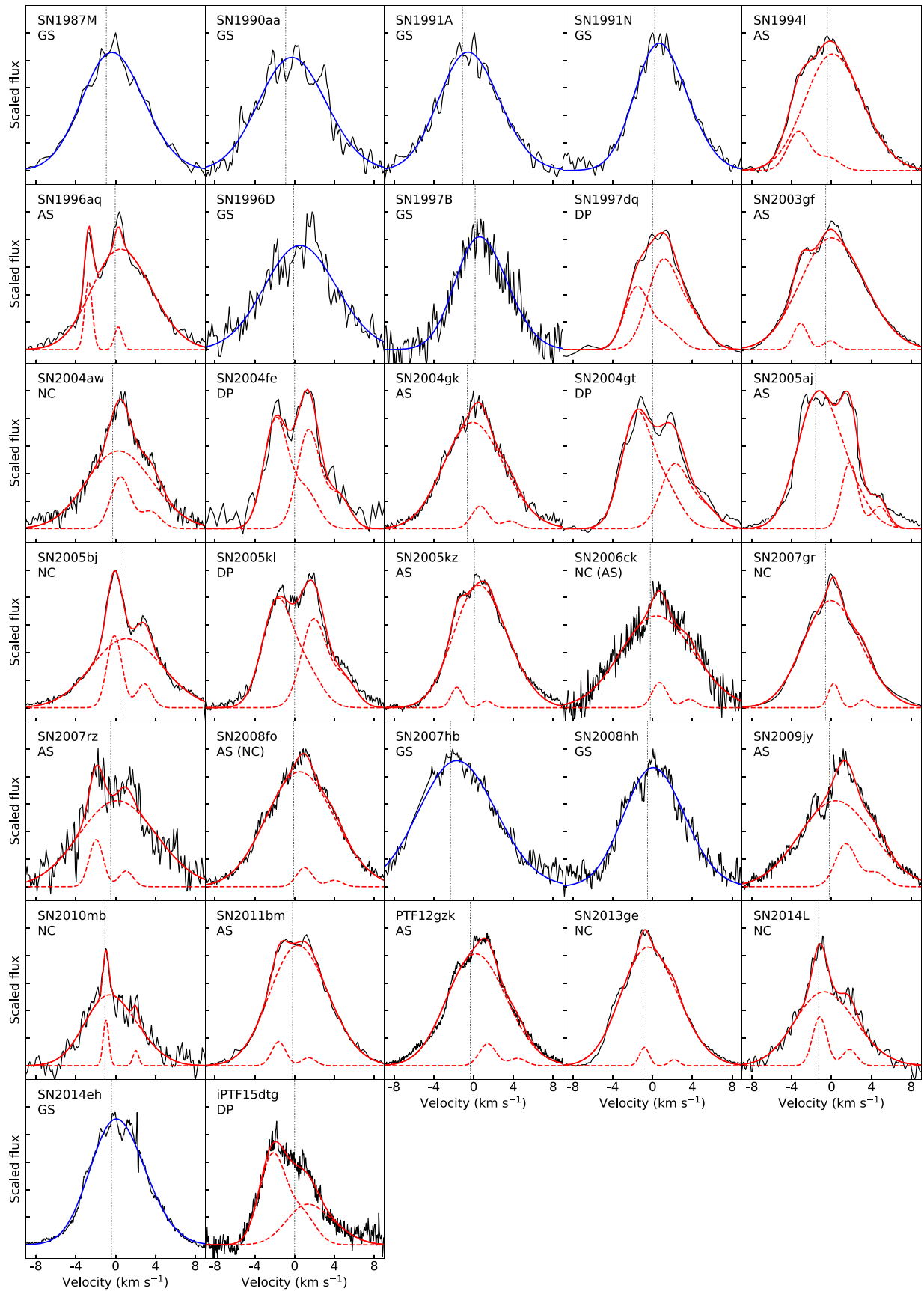


**Figure B3.** Observed [O I] of the SNe Ic in the sample fitted by multi-Gaussians. The spectra (black solid lines) are already subtracted by the background and the symmetric  $H\alpha/[N II]$ . The blue solid lines are the results of a one-component fit. The red solid lines are the results of a two-component fit, and the red dashed lines are the components. The vertical dotted lines are zero velocity ( $6300 \text{ \AA}$ ) for DP objects or the center wavelength of the Gaussian broad base for GS, NC, or AS objects for reference.

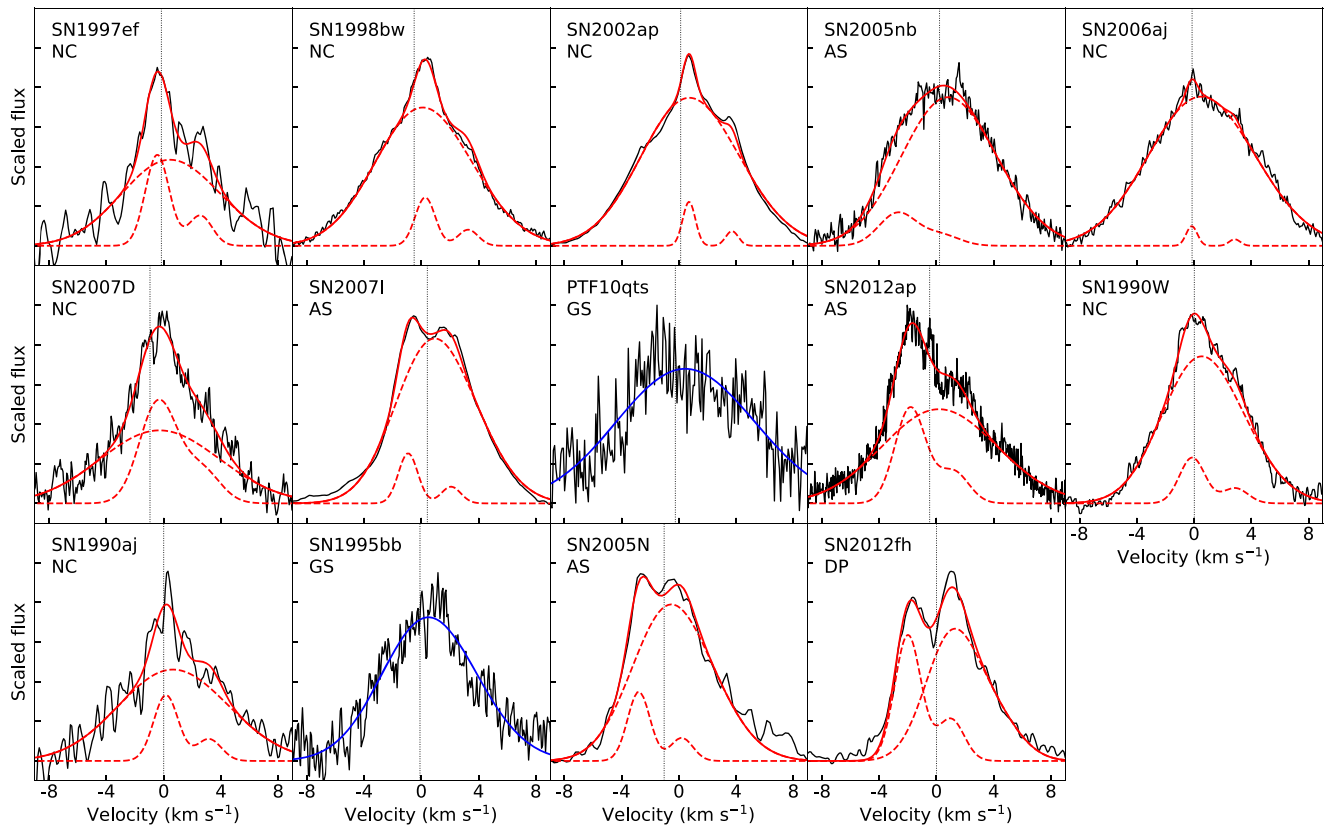


**Figure B4.** Observed [O I] of the SNe Ic-BL and SNe Ib/c in the sample fitted by multi-Gaussians. The spectra (black solid lines) are already subtracted by the background and the symmetric  $H\alpha/[N II]$ . The blue solid lines are the results of a one-component fit. The red solid lines are the results of a two-component fit, and the red dashed lines are the components. The vertical dotted lines are zero velocity ( $6300 \text{ \AA}$ ) for DP objects or the center wavelength of the Gaussian broad base for GS, NC, or AS objects for reference.

### Appendix C Examples of Multiphase Nebular Spectra

In this section, we show a direct comparison of the nebular spectra at different phases for the well-observed SNe in this sample (Figure C1)

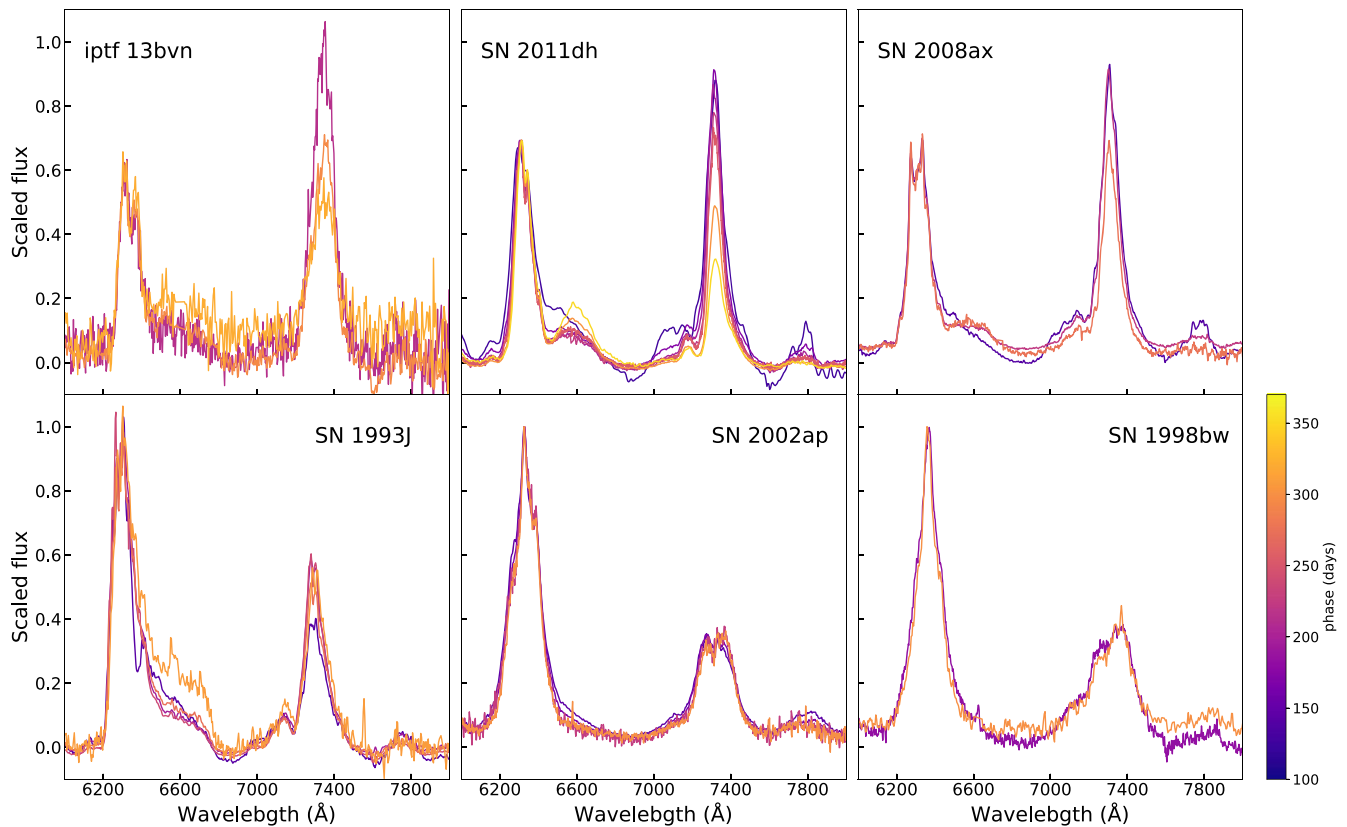


**Figure C1.** The evolution of  $[\text{O I}]/[\text{Ca II}]$  of well-observed SNe. The spectra are scaled to the peak of the  $[\text{O I}]$ . The colors of the lines indicate the phase of the spectra, with the late-phase spectra plotted with the colors at the red end. The SNe with spectra plotted in the upper panels have fast evolving  $[\text{O I}]/[\text{Ca II}]$  and relatively low  $[\text{O I}]/[\text{Ca II}]$  ( $<1$ ) at  $\sim 200$  days. The SNe with spectra plotted in the lower panels are examples with relatively large  $[\text{O I}]/[\text{Ca II}]$  ( $>1.5$ ), and their  $[\text{O I}]/[\text{Ca II}]$  hardly evolve from 100 to 350 days.

### ORCID iDs

Qiliang Fang (方其亮) <https://orcid.org/0000-0002-1161-9592>  
 Keiichi Maeda <https://orcid.org/0000-0003-2611-7269>  
 Hanindyo Kuncarayakti <https://orcid.org/0000-0002-1132-1366>  
 Masaomi Tanaka <https://orcid.org/0000-0001-8253-6850>  
 Koji S. Kawabata <https://orcid.org/0000-0001-6099-9539>  
 Takashi Hattori <https://orcid.org/0000-0002-8996-7562>  
 Takashi J. Moriya <https://orcid.org/0000-0003-1169-1954>

### References

- Astropy Collaboration, Price-Whelan, A. M., Sipőcz, B. M., et al. 2018, *AJ*, **156**, 123
- Astropy Collaboration, Robitaille, T. P., Tollerud, E. J., et al. 2013, *A&A*, **558**, A33
- Barbon, R., Benetti, S., Cappellaro, E., et al. 1995, *A&AS*, **110**, 513
- Ben-Ami, S., Gal-Yam, A., Mazzali, P. A., et al. 2014, *ApJ*, **785**, 37
- Benetti, S., Turatto, M., Valenti, S., et al. 2011, *MNRAS*, **411**, 2726
- Blondin, S., Modjaz, M., Kirshner, R., et al. 2007, *CBE Telegram*, **808**, 1
- Bufano, F., Pignata, G., Bersten, M., et al. 2014, *MNRAS*, **439**, 1807
- Cao, Y., Kasliwal, M. M., Arcavi, I., et al. 2013, *ApJL*, **775**, L7
- Cardelli, J. A., Clayton, G. C., & Mathis, J. S. 1989, *ApJ*, **345**, 245
- Chornock, R., Filippenko, A. V., Li, W., et al. 2011, *ApJ*, **739**, 41
- Clocchiatti, A., Suntzeff, N. B., Covarrubias, R., et al. 2011, *AJ*, **141**, 163
- Colesanti, C., Jacques, C., Pimentel, E., et al. 2006, *IAU Circ.*, **8713**, 1
- Collins, C., Müller, B., & Heger, A. 2018, *MNRAS*, **473**, 1695
- Dessart, L., & Hillier, D. J. 2020, *A&A*, **642**, A33
- Dessart, L., Hillier, D. J., Sukhbold, T., et al. 2021, *A&A*, **656**, A61
- Dessart, L., Hillier, D. J., Woosley, S., et al. 2016, *MNRAS*, **458**, 1618
- Dessart, L., John Hillier, D., Sukhbold, T., et al. 2021, *A&A*, **652**, A64
- Dessart, L., Yoon, S.-C., Aguilera-Dena, D. R., et al. 2020, *A&A*, **642**, A106
- Drissen, L., Robert, C., Dutil, Y., et al. 1996, *IAU Circ.*, **6317**, 2
- Drout, M. R., Milisavljevic, D., Parrent, J., et al. 2016, *ApJ*, **821**, 57
- Drout, M. R., Soderberg, A. M., Gal-Yam, A., et al. 2011, *ApJ*, **741**, 97
- Elmhamdi, A., Danziger, I. J., Cappellaro, E., et al. 2004, *A&A*, **426**, 963
- Elmhamdi, A., Tsvetkov, D., Danziger, I. J., et al. 2011, *ApJ*, **731**, 129
- Ergon, M., Jerkstrand, A., Sollerman, J., et al. 2015, *A&A*, **580**, A142
- Ergon, M., Sollerman, J., Fraser, M., et al. 2014, *A&A*, **562**, A17
- Evans, R., Sadler, E., & McNaught, R. H. 1990, *IAU Circ.*, **5076**, 1
- Fang, Q., & Maeda, K. 2018, *ApJ*, **864**, 47
- Fang, Q., Maeda, K., Kuncarayakti, H., et al. 2019, *NatAs*, **3**, 434
- Filippenko, A. V. 1988, *AJ*, **96**, 1941
- Filippenko, A. V., Barth, A. J., Matheson, T., et al. 1995, *ApJL*, **450**, L11
- Filippenko, A. V., Foley, R. J., & Matheson, T. 2005, *IAU Circ.*, **8639**, 2
- Filippenko, A. V., & Korth, S. 1991, *IAU Circ.*, **5234**, 1
- Filippenko, A. V., Porter, A. C., & Sargent, W. L. W. 1990, *AJ*, **100**, 1575
- Filippenko, A. V., & Sargent, W. L. W. 1986, *AJ*, **91**, 691
- Folatelli, G., Bersten, M. C., Kuncarayakti, H., et al. 2014, *ApJ*, **792**, 7
- Folatelli, G., Bersten, M. C., Kuncarayakti, H., et al. 2015, *ApJ*, **811**, 147
- Folatelli, G., Contreras, C., Phillips, M. M., et al. 2006, *ApJ*, **641**, 1039
- Foley, R. J., Papenkova, M. S., Swift, B. J., et al. 2003, *PASP*, **115**, 1220
- Fransson, C., & Chevalier, R. A. 1989, *ApJ*, **343**, 323
- Fremming, C., Sollerman, J., Taddia, F., et al. 2016, *A&A*, **593**, A68
- Galama, T. J., Vreeswijk, P. M., van Paradijs, J., et al. 1998, *Natur*, **395**, 670
- Gal-Yam, A., Fox, D. B., Kulkarni, S. R., et al. 2005, *ApJL*, **630**, L29
- Gómez, G., & López, R. 1994, *AJ*, **108**, 195
- Gómez, G., & López, R. 2002, *AJ*, **123**, 328
- Green, D. W. E. 2006, *CBE Telegram*, **368**, 2
- Groh, J. H., Georgy, C., & Ekström, S. 2013, *A&A*, **558**, L1
- Guillochon, J., Parent, J., Kelley, L. Z., et al. 2017, *ApJ*, **835**, 64
- Hamuy, M., Deng, J., Mazzali, P. A., et al. 2009, *ApJ*, **703**, 1612
- Harris, C. R., Millman, K. J., van der Walt, S. J., et al. 2020, *Natur*, **585**, 357
- Harutyunyan, A. H., Pfahler, P., Pastorello, A., et al. 2008, *A&A*, **488**, 383
- Heger, A., Fryer, C. L., Woosley, S. E., et al. 2003, *ApJ*, **591**, 288
- Hjorth, J., Sollerman, J., Møller, P., et al. 2003, *Natur*, **423**, 847
- Holland-Ashford, T., Lopez, L. A., Auchettl, K., et al. 2017, *ApJ*, **844**, 84
- Hunter, J. D. 2007, *CSE*, **9**, 90
- Iwamoto, K., Nakamura, T., Nomoto, K., et al. 2000, *ApJ*, **534**, 660
- Jeffery, D. J., Branch, D., Filippenko, A. V., et al. 1991, *ApJL*, **377**, L89

- Jerkstrand, A. 2017, *Handbook of Supernovae* (Cham: Springer), 795
- Jerkstrand, A., Ergon, M., Smartt, S. J., et al. 2015, *A&A*, 573, A12
- Kashikawa, N., Aoki, K., Asai, R., et al. 2002, *PASJ*, 54, 819
- Katsuda, S., Morii, M., Janka, H.-T., et al. 2018, *ApJ*, 856, 18
- Kilpatrick, C. D., Drout, M. R., Auchettl, K., et al. 2021, *MNRAS*, 504, 2073
- Kilpatrick, C. D., Foley, R. J., Abramson, L. E., et al. 2017, *MNRAS*, 465, 4650
- Kuncarayakti, H., Maeda, K., Bersten, M. C., et al. 2015, *A&A*, 579, A95
- Li, H., & McCray, R. 1996, *ApJ*, 456, 370
- Limongi, M., & Chieffi, A. 2003, *ApJ*, 592, 404
- Loader, C. 1999, *Local Regression and Likelihood* (New York: Springer)
- Loader, C. 2018, *locfit: Local Regression, Likelihood and Density Estimation*, <https://cran.r-project.org/web/packages/locfit/locfit.pdf>
- Lyman, J. D., Bersier, D., James, P. A., et al. 2016, *MNRAS*, 457, 328
- Maeda, K., Hattori, T., Milisavljevic, D., et al. 2015, *ApJ*, 807, 35
- Maeda, K., Kawabata, K., Mazzali, P. A., et al. 2008, *Sci*, 319, 1220
- Maeda, K., Mazzali, P. A., & Nomoto, K. 2006, *ApJ*, 645, 1331
- Maeda, K., Nakamura, T., Nomoto, K., et al. 2002, *ApJ*, 565, 405
- Maeda, K., & Nomoto, K. 2003, *ApJ*, 598, 1163
- Maeda, K., Nomoto, K., Mazzali, P. A., et al. 2006, *ApJ*, 640, 854
- Makarov, D., Prugniel, P., Terekhova, N., et al. 2014, *A&A*, 570, A13
- Matheson, T., Filippenko, A. V., Ho, L. C., et al. 2000, *AJ*, 120, 1499
- Matheson, T., Filippenko, A. V., Li, W., et al. 2001, *AJ*, 121, 1648
- Maund, J. R., Fraser, M., Ergon, M., et al. 2011, *ApJL*, 739, L37
- Maund, J. R., Smartt, S. J., Kudritzki, R. P., et al. 2004, *Natur*, 427, 129
- Maund, J. R., Wheeler, J. C., Patat, F., et al. 2007, *ApJ*, 671, 1944
- Maurer, J. I., Mazzali, P. A., Deng, J., et al. 2010, *MNRAS*, 402, 161
- Mazzali, P. A., Deng, J., Maeda, K., et al. 2002, *ApJL*, 572, L61
- Mazzali, P. A., Iwamoto, K., & Nomoto, K. 2000, *ApJ*, 545, 407
- Mazzali, P. A., Kawabata, K. S., Maeda, K., et al. 2005, *Sci*, 308, 1284
- Milisavljevic, D., Fesen, R. A., Gerardy, C. L., et al. 2010, *ApJ*, 709, 1343
- Milisavljevic, D., Margutti, R., Kamble, A., et al. 2015, *ApJ*, 815, 120
- Milisavljevic, D., Margutti, R., Parent, J. T., et al. 2015, *ApJ*, 799, 51
- Milisavljevic, D., Margutti, R., Soderberg, A. M., et al. 2013, *ApJ*, 767, 71
- Milisavljevic, D., Soderberg, A. M., Margutti, R., et al. 2013, *ApJL*, 770, L38
- Modjaz, M. 2007, PhD thesis, Harvard Univ.
- Modjaz, M., Blondin, S., Kirshner, R. P., et al. 2014, *AJ*, 147, 99
- Modjaz, M., Kirshner, R. P., Blondin, S., et al. 2008, *ApJL*, 687, L9
- Modjaz, M., Li, W., Butler, N., et al. 2009, *ApJ*, 702, 226
- Modjaz, M., Liu, Y. Q., Bianco, F. B., et al. 2016, *ApJ*, 832, 108
- Modjaz, M., Stanek, K. Z., Garnavich, P. M., et al. 2006, *ApJL*, 645, L21
- Morales-Garoffolo, A., Elias-Rosa, N., Benetti, S., et al. 2014, *MNRAS*, 445, 1647
- Morales-Garoffolo, A., Elias-Rosa, N., Bersten, M., et al. 2015, *MNRAS*, 454, 95
- Müller, B., Heger, A., Liptai, D., et al. 2016, *MNRAS*, 460, 742
- Nagao, T., Patat, F., Taubenberger, S., et al. 2021, *MNRAS*, 505, 3664
- Nakamura, T., Mazzali, P. A., Nomoto, K., et al. 2001, *ApJ*, 550, 991
- Nakano, S., Aoki, M., Jha, S., et al. 1997, *IAU Circ.*, 6770, 2
- Nakano, S., Aoki, M., Kushida, R., et al. 1996, *IAU Circ.*, 6454, 1
- Park, T., Kashyap, V. L., Siemiginowska, A., et al. 2006, *ApJ*, 652, 610
- Patat, F., Cappellaro, E., Danziger, J., et al. 2001, *ApJ*, 555, 900
- Patat, F., Chugai, N., & Mazzali, P. A. 1995, *A&A*, 299, 715
- Prentice, S. J., Mazzali, P. A., Pian, E., et al. 2016, *MNRAS*, 458, 2973
- Qiu, Y., Li, W., Qiao, Q., et al. 1999, *AJ*, 117, 736
- Quimby, R., Mondol, P., Castro, F., et al. 2006, *IAU Circ.*, 8657, 1
- R Core Team 2021, *R: A Language and Environment for Statistical Computing* (Vienna), <https://www.R-project.org>
- Richmond, M. W., van Dyk, S. D., Ho, W., et al. 1996, *AJ*, 111, 327
- Roy, R., Kumar, B., Maund, J. R., et al. 2013, *MNRAS*, 434, 2032
- Sahu, D. K., Gurugubelli, U. K., Anupama, G. C., et al. 2011, *MNRAS*, 413, 2583
- Shivvers, I., Filippenko, A. V., Silverman, J. M., et al. 2019, *MNRAS*, 482, 1545
- Shivvers, I., Mazzali, P., Silverman, J. M., et al. 2013, *MNRAS*, 436, 3614
- Shivvers, I., Modjaz, M., Zheng, W., et al. 2017, *PASP*, 129, 054201
- Silverman, J. M., Mazzali, P., Chornock, R., et al. 2009, *PASP*, 121, 689
- Smartt, S. J. 2009, *ARA&A*, 47, 63
- Smartt, S. J. 2015, *PASA*, 32, e016
- Smith, N. 2014, *ARA&A*, 52, 487
- Stritzinger, M., Mazzali, P., Phillips, M. M., et al. 2009, *ApJ*, 696, 713
- Sukhbold, T., Ertl, T., Woosley, S. E., et al. 2016, *ApJ*, 821, 38
- Taddia, F., Fremling, C., Sollerman, J., et al. 2016, *A&A*, 592, A89
- Taddia, F., Sollerman, J., Fremling, C., et al. 2019, *A&A*, 621, A64
- Taddia, F., Stritzinger, M. D., Bersten, M., et al. 2018, *A&A*, 609, A136
- Tartaglia, L., Fraser, M., Sand, D. J., et al. 2017, *ApJL*, 836, L12
- Taubenberger, S., Navasardyan, H., Maurer, J. I., et al. 2011, *MNRAS*, 413, 2140
- Taubenberger, S., Pastorello, A., Mazzali, P. A., et al. 2006, *MNRAS*, 371, 1459
- Taubenberger, S., Valenti, S., Benetti, S., et al. 2009, *MNRAS*, 397, 677
- Tody, D. 1986, *Proc. SPIE*, 627, 733
- Tody, D. 1993, in *ASP Conf. Ser. 52, Astronomical Data Analysis Software and Systems II*, ed. R. J. Hanisch (San Francisco, CA: ASP), 173
- Turatto, M., Benetti, S., & Cappellaro, E. 2003, in *From Twilight to Highlight: The Physics of Supernovae*, ed. W. Hillebrandt & B. Leibundgut (Berlin: Springer), 200
- Ugliano, M., Janka, H.-T., Marek, A., et al. 2012, *ApJ*, 757, 69
- Valenti, S., Fraser, M., Benetti, S., et al. 2011, *MNRAS*, 416, 3138
- Valenti, S., Taubenberger, S., Pastorello, A., et al. 2012, *ApJL*, 749, L28
- van Dokkum, P. G. 2001, *PASP*, 113, 1420
- Van Dyk, S. D., Zheng, W., Fox, O. D., et al. 2014, *AJ*, 147, 37
- Virtanen, P., Gommers, R., Oliphant, T. E., et al. 2020, *NatMe*, 17, 261
- Walker, E. S., Mazzali, P. A., Pian, E., et al. 2014, *MNRAS*, 442, 2768
- Wang, L., Howell, D. A., Höflich, P., et al. 2001, *ApJ*, 550, 1030
- Wang, L., & Wheeler, J. C. 2008, *ARA&A*, 46, 433
- Wheeler, J. C., Harkness, R. P., Clocchiatti, A., et al. 1994, *ApJL*, 436, L135
- Woosley, S. E., & Bloom, J. S. 2006, *ARA&A*, 44, 507
- Woosley, S. E., Heger, A., & Weaver, T. A. 2002, *RvMP*, 74, 1015
- Yaron, O., & Gal-Yam, A. 2012, *PASP*, 124, 668
- Yoon, S.-C. 2015, *PASA*, 32, e015
- Yoshida, M., Shimizu, Y., Sasaki, T., et al. 2000, *Proc. SPIE*, 4009, 240
- Yoshii, Y., Tomita, H., Kobayashi, Y., et al. 2003, *ApJ*, 592, 467
- Zhang, J., Wang, X., Vinkó, J., et al. 2018, *ApJ*, 863, 109